Floquet scattering and classical-quantum correspondence in strong time-periodic fields

Agapi Emmanouilidou and L. E. Reichl
Center for Studies in Statistical Mechanics and Complex Systems, The University of Texas at Austin, Austin, Texas 78212
(Received 18 June 2001; published 7 February 2002)

We study the scattering of an electron from a one-dimensional inverted Gaussian atomic potential in the presence of strong time-periodic electric fields. Using Floquet theory, we construct the Floquet scattering matrix in the Kramers-Henneberger frame. We compute the transmission coefficients as a function of electron incident energy and find that they display asymmetric Fano resonances due to the electron interaction with the driving field. We find that the Fano resonances are associated with zero-pole pairs of the Floquet scattering matrix in the complex energy plane. Another way we ''probe'' the complex spectrum of the system is by computing the Wigner-Smith delay times. Finally, we find that the eigenphases of the Floquet scattering matrix undergo a number of ''avoided crossings'' as a function of electron Floquet energy, and this number increases with increasing strength of the driving field. These ''avoided crossings'' appear to be quantum manifestations of the destruction of the constants of motion and the onset of chaos in classical phase space.

DOI: 10.1103/PhysRevA.65.033405 PACS number(s): 34.50.Rk, 32.80.−t, 03.65.Nk, 05.45.Mt

I. INTRODUCTION

The development of ultrahigh-intensity lasers has led to the study of atoms in external time-periodic electric fields that are comparable in strength to the electric fields produced by the atomic nucleus. One of the most interesting phenomena observed in these time-periodic systems is the stabilization with increasing laser intensity that was predicted theoretically [1–3] and has been verified experimentally [4,5].

In previous studies, one-dimensional atomic potentials have been used to predict several phenomena in the theory of laser-atom interactions at high laser intensities. Many of these studies were carried out in the context of Floquet theory formulated in the Kramers-Henneberger (KH) frame of reference [6,7], which oscillates with a free electron in the time-periodic field. Gavrila and Kaminski [1] developed a nonperturbative method to study electron scattering in the presence of strong time-periodic electric fields. Using three-dimensional models, Dimou and Faisal [8] as well as Collins and Csanak [8] have studied resonances in laser-assisted scattering. Bhatt, Piraux, and Burnett [9], in their work on electron scattering from a polarization potential in the presence of strong monochromatic light, argued the appearance of new light-induced quasibound states (resonances) as the field strength is increased. The same phenomenon was later also observed by Bardsley and Comella [10] and Yao and Chu [11], who used the complex coordinate scaling transformation to compute the complex quasibound states in their study of photodetachment from a one-dimensional Gaussian potential. In addition, the same atomic potential was used by Marinescu and Gavrila [12] to compare the predictions of the full Floquet theory with those of the high-frequency Floquet theory (HFFT), using resonance (Siegert) boundary conditions. (The HFFT theory is a version of the Floquet approach adapted to treat the high-frequency limit.) Recently, Timberlake and Reichl [13], using the inverted Gaussian potential, studied the phase-space picture of resonance creation and they showed that the light-induced quasibound states are scarred on unstable periodic orbits of the classical motion.

In this paper, we study the scattering of an electron from a short-range atomic potential in the presence of a strong time-periodic electric field. The atomic potential we consider is the one-dimensional inverted Gaussian potential, a model that has already offered interesting insights into different aspects of the laser-atom interactions [10–12]. Our goal is to construct the Floquet scattering matrix ($\boldsymbol{S}$ matrix) using the full Floquet theory formulated in the KH frame for a strongly driven atomic system. A Floquet scattering matrix has been constructed by Li and Reichl [14] for periodically driven mesoscopic systems. The Floquet $\boldsymbol{S}$-matrix connects the outgoing propagating modes to the incoming propagating modes and is a unitary matrix that conserves probability. We construct the Floquet $\boldsymbol{S}$ matrix in the KH frame, where we can define asymptotic states.

In Sec. II, we construct the Floquet $\boldsymbol{S}$ matrix in the KH frame. In Sec. III A, we compute the transmission coefficients and the poles of the Floquet $\boldsymbol{S}$ matrix and find the quasibound states of the atomic system. In Sec. III B, we compute the Wigner-Smith delay times of the scattered electron as a function of the electron incident energy and show that the Wigner-Smith delay times of the scattered electron due to the presence of the quasibound states are of the same order of magnitude as the lifetimes obtained from the poles of the Floquet $\boldsymbol{S}$ matrix. We finish, in Sec. III C, with a quite interesting observation. When plotting the eigenphases of the unitary Floquet $\boldsymbol{S}$ matrix as a function of the electron's Floquet energy we find that at certain energies the eigenphases undergo ''avoided crossings'' that change the eigenphases character completely. We find that the number of ''avoided crossings'' increases with increasing strength of the time-periodic electric field. The ''avoided crossings'' observed as the strength of the driving field is increased appear to be quantum manifestations of the destruction of the Kolmogorov-Arnold-Moser (KAM) surfaces and the onset of chaos in the classical phase space.

II. THE FLOQUET *S* MATRIX

A. The model

We study the scattering of an electron in the presence of a strong electric field and a short-range atomic potential. The

electric field $E(t)=E_0\sin(\omega t)(T=2\pi/\omega$ is the period of the field) is treated within the dipole approximation as a monochromatic infinite plane wave linearly polarized along the direction of the incident electron. The Schrödinger equation, in one space dimension x, that describes the dynamics of the system is in atomic units (a.u.)

$$i\frac{\partial\Psi(x,t)}{\partial t}=\left[\frac{1}{2}\left(-i\frac{\partial}{\partial x}-qA(t)\right)^2+V(x)\right]\Psi(x,t), \quad (1)$$

where $V(x)$ is the inverted Gaussian potential,

$$V(x)=-V_0e^{-(x/\delta)^2}, \quad (2)$$

and q is the particle charge which for the electron is $q=-1$ a.u. The electric field is, $E(t)=-\partial A(t)/\partial t$, where $A(t)$ is the vector potential and is given by

$$A(t)=\frac{E_0}{\omega}\cos(\omega t). \quad (3)$$

We use atomic units ($e=\hbar=m=1$) throughout this paper, except when otherwise indicated.

To construct the Floquet $\boldsymbol{S}$ matrix of the system, we transform to the KH frame [6,7]. In the KH frame there are well-defined asymptotic regions and the boundary conditions are expressed in terms of free electron waves. To obtain the wave function in the KH frame, we introduce the unitary transformation [6,7]

$$\Phi(x,t)=U_1U_2\Psi(x,t), \quad (4)$$

where

$$U_1=\exp\left(\frac{iq^2}{2}\int_{-\infty}^{t}A^2(t')dt'\right)$$

and

$$U_2=\exp\left(-q\int_{-\infty}^{t}A(t')\frac{\partial}{\partial x}dt'\right). \quad (5)$$

U_1 is a phase transformation to remove the A^2 term from Eq. (1) while U_2 is a space-translation transformation to the KH frame. In the KH frame, the wave function satisfies the following Schrödinger equation:

$$i\frac{\partial\Phi(x,t)}{\partial t}=\left(-\frac{1}{2}\frac{\partial^2}{\partial x^2}+V(x+a(t))\right)\Phi(x,t), \quad (6)$$

where $a(t)$ is the classical displacement of a free electron from its center of oscillation in the time-periodic field $E(t)$, and is given by

$$a(t)=-q\int_{-\infty}^{t}A(t')dt'=a_0\sin(\omega t)$$

with

$$a_0=-qE_0/\omega^2. \quad (7)$$

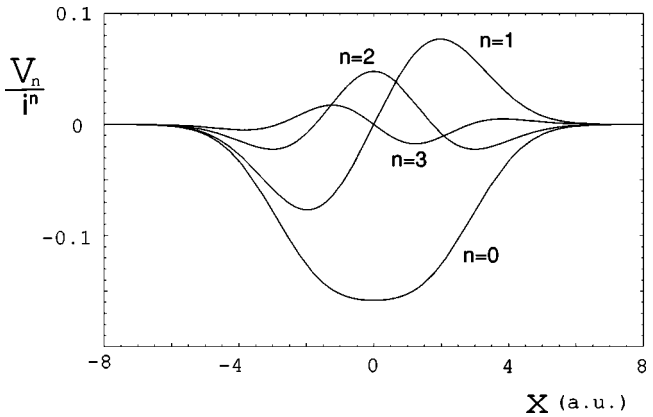

FIG. 1. The Fourier components $V_n(\alpha_0;x)/i^n$ (a.u.) of the inverted Gaussian potential as a function of the one space dimension x(a.u.) in the KH frame, for $\alpha_0=2.25$ a.u.

In Eq. (6), the potential is a periodic function of time, that is $V(x+a(t))=V(x+a(t+T))$. Thus, according to the Floquet theorem [15], Eq. (6) has solutions of the form

$$\Phi_{\mathcal{E}}(x,t)=e^{-i\mathcal{E}t}\phi_{\mathcal{E}}(x,t), \quad (8)$$

where $\mathcal{E}$ is the Floquet energy, $\mathcal{E}\in[0,\omega)$, and $\phi_{\mathcal{E}}(x,t)$ is a periodic function of time, $\phi_{\mathcal{E}}(x,t)=\phi_{\mathcal{E}}(x,t+T)$. Taking the Fourier expansion of $\phi_{\mathcal{E}}(x,t)$, we obtain

$$\Phi_{\mathcal{E}}(x,t)=e^{-i\mathcal{E}t}\sum_{n=-\infty}^{+\infty}\phi_n(x)e^{-in\omega t}, \quad (9)$$

where n indicates the Floquet channel. Note that $\phi_n(x)$ is also $\mathcal{E}$ dependent, but we omit the $\mathcal{E}$ subscript to simplify notation. The energy E of an incident electron in the KH frame is related to the Floquet energy through the expression $E=\mathcal{E}+n\omega$. Next, we Fourier analyze the potential

$$V(x+a(t))=\sum_{n=-\infty}^{+\infty}V_n(a_0;x)e^{-i\omega t}, \quad (10)$$

where the Fourier components for the inverted Gaussian potential, Eq. (2), can be written as

$$V_n(a_0;x)=\frac{1}{2\pi}\int_0^{2\pi}V(x+a(t))e^{in\omega t}d(\omega t)$$

$$=-V_0\frac{i^n}{\pi}\int_0^{\pi}\cos(n\omega t)e^{-(x+a_0\cos(\omega t))^2/\delta^2}d(\omega t), \quad (11)$$

see Fig. 1. To be able to construct the Floquet $\boldsymbol{S}$ matrix, the Fourier components $V_n(a_0;x)$ must be smooth functions in the one space dimension x in the KH frame. This is indeed the case for the inverted Gaussian potential, Eq. (11). Note that in the KH frame, the potential oscillates back and forth along the x axis (laterally) with the period of the external field.

From Eq. (11), we see that the components $V_n(\alpha_0;x)$ of the atomic potential in the limit $x\to\pm\infty$ tend to zero faster

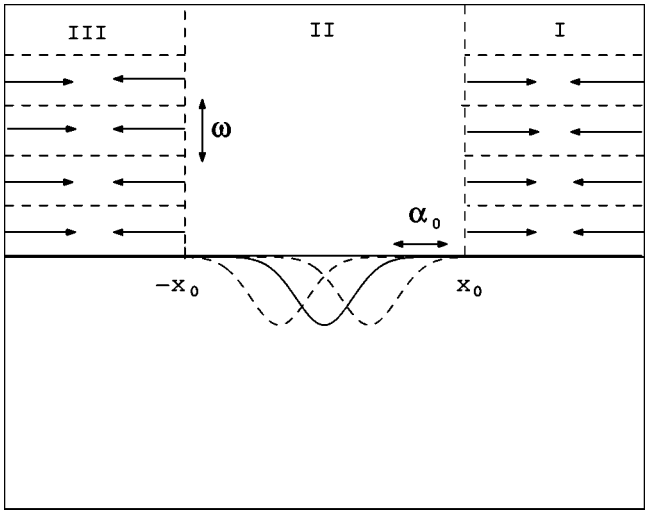

FIG. 2. Not drawn to scale, are shown in the KH frame, the asymptotic regions I $x\in[x_0,+\infty)$(a.u.) and III $x\in(-\infty,-x_0]$(a.u.), where the potential is asymptotically zero, and the scattering region II, where the inverted Gaussian potential oscillates laterally. In regions I and III, we also show the Floquet channels, denoted by dotted lines, and the incoming and outgoing electron waves, denoted by solid arrows.

than $1/x$ and we can thus divide the one space dimension x in three regions: the asymptotic regions I, $x\in[x_0,\infty)$, and III, $x\in(-\infty,-x_0]$, where the potential is asymptotically zero; and the scattering region II, $x\in[-x_0,x_0]$, where the potential $V(x+\alpha(t))$ is not zero, see Fig. 2. In the rest of this paper, for brevity, we refer to the potential in asymptotic regions I and III as being zero instead of asymptotically zero. The choice of x_0 depends on the value of the parameter α_0. The larger α_0 is, the further out we have to define the asymptotic regions I and III.

B. Floquet solution in the scattering region II

Substituting Eqs. (9) and (10) into Eq. (6), we obtain an infinite system of coupled differential equations [1] for the Floquet components $\phi_n(x)$,

$$-\frac{1}{2}\frac{d^2}{dx^2}\phi_n(x)+[V_0(\alpha_0;x)-(\mathcal{E}+n\omega)]\phi_n(x)+\sum_{\substack{l=-\infty\\ l\neq n}}^{+\infty}V_{n-l}(\alpha_0;x)\phi_l(x)=0. \tag{12}$$

Next, we truncate to a finite number of Floquet channels and take n_e and n_p to be the lower and upper limit of the Floquet channels considered. That is, $n=-n_e,\ldots,0,\ldots,n_p$ and the total number of Floquet channels is given by $N=n_e+n_p+1$. After truncating, Eq. (12) can be cast in the following matrix form:

$$\boldsymbol{I}\frac{d^2}{dx^2}\boldsymbol{\phi}^{II}(x)=\boldsymbol{M}(x)\boldsymbol{\phi}^{II}(x), \tag{13}$$

where $\boldsymbol{I}$ is the unit $N\times N$ matrix, $\boldsymbol{\phi}^{II}(x)$ is the $N\times 1$ matrix with elements $\boldsymbol{\phi}^{II}_n(x)=\phi_n(x)$ and $\boldsymbol{M}(x)$ is an $N\times N$ matrix with elements

$$\boldsymbol{M}_{n,l}(x)=2[V_{n-l}(\alpha_0;x)-\delta_{n,l}(\mathcal{E}+n\omega)], \tag{14}$$

where $\delta_{n,l}$ is the Kronecker delta and $n,l=-n_e,\ldots,0,\ldots,n_p$. The general solution of the second-order N-coupled differential equations, Eq. (13), can be written as a linear combination of $2N$ linearly independent columns $\boldsymbol{\chi}_j(x)$, with $j=1,\ldots,2N$, as follows,

$$\begin{aligned}\boldsymbol{\phi}^{II}(x)&=c_1\boldsymbol{\chi}_1(x)+c_2\boldsymbol{\chi}_2(x)+\cdots+c_N\boldsymbol{\chi}_N(x)+d_1\boldsymbol{\chi}_{N+1}(x)\\&\quad+d_2\boldsymbol{\chi}_{N+2}(x)+\cdots+d_N\boldsymbol{\chi}_{2N}(x)\\&\equiv\boldsymbol{X}^{(1)}(x)\boldsymbol{C}+\boldsymbol{X}^{(2)}(x)\boldsymbol{D},\end{aligned} \tag{15}$$

where $\boldsymbol{X}^{(1)}(x)$ and $\boldsymbol{X}^{(2)}(x)$ are $N\times N$ matrices whose elements are functions of the one space dimension x and $\boldsymbol{C}$, $\boldsymbol{D}$ are constant $N\times 1$ matrices. Each of the linearly independent columns $\boldsymbol{\chi}_j(x)$ satisfies Eq. (13)

$$\boldsymbol{I}\frac{d^2}{dx^2}\boldsymbol{\chi}_j(x)=\boldsymbol{M}(x)\boldsymbol{\chi}_j(x)\Rightarrow\frac{d^2}{dx^2}\chi_{n,j}(x)=\sum_{l=-n_e}^{n_p}\boldsymbol{M}_{n,l}(x)\chi_{l,j}(x), \tag{16}$$

where $n=-n_e,\ldots,0,\ldots,n_p$ and $j=1,\ldots,2N$. The functions $\chi_{n,j}(x)$ can be found analytically if the matrix elements of $\boldsymbol{M}(x)$ are constant. From Eq. (15), it follows that every channel function $\phi^{II}_n(x)$ can be written as a linear combination of $2N$ functions $\chi_{n,j}(x)$ and thus, the wave function in the scattering region II is given by

$$\Phi^{II}_{\mathcal{E}}(x,t)=\sum_{n=-n_e}^{n_p}\sum_{m=1}^{N}[\chi_{n,m}(x)c_m+\chi_{n,N+m}(x)d_m]e^{-i\mathcal{E}t}e^{-in\omega t}. \tag{17}$$

C. Floquet solution in the asymptotic regions

In the asymptotic regions I and III, the potential $V(x+\alpha(t))$ is zero. Thus, we can consider as our boundary conditions a superposition of incoming and outgoing free-electron waves in the N truncated Floquet channels that are incident from both sides of the scattering region,

$$\begin{aligned}\Phi^{I}_{\mathcal{E}}(x,t)&=\sum_{n=-n_e}^{n_p}\phi^{I}_n(x)e^{-i\mathcal{E}t}e^{-in\omega t}\\&=\sum_{n=-n_e}^{n_p}b_n^{out}\frac{e^{ik_nx}}{\sqrt{k_n}}e^{-i\mathcal{E}t}e^{-in\omega t}+\sum_{n=-n_e}^{n_p}b_n^{in}\frac{e^{-ik_nx}}{\sqrt{k_n}}e^{-i\mathcal{E}t}e^{-in\omega t},\end{aligned} \tag{18}$$

$$\Phi_{\mathcal{E}}^{III}(x,t)=\sum_{n=-n_e}^{n_p}\phi_n^{III}(x)e^{-i\mathcal{E}t}e^{-in\omega t}$$
$$=\sum_{n=-n_e}^{n_p}a_n^{out}\frac{e^{-ik_nx}}{\sqrt{k_n}}e^{-i\mathcal{E}t}e^{-in\omega t}$$
$$+\sum_{n=-n_e}^{n_p}a_n^{in}\frac{e^{ik_nx}}{\sqrt{k_n}}e^{-i\mathcal{E}t}e^{-in\omega t}, \quad (19)$$

where b_n^{in}, a_n^{in} and b_n^{out}, a_n^{out} are the probability amplitudes of the incoming and outgoing electron waves, respectively, that are incident in the nth Floquet channel with energy $E=\mathcal{E}+n\omega$, see Fig. 2. Propagating modes are incident on the Floquet channels $n=0,\ldots,n_p$ and have wave vectors $k_n=\sqrt{2(\mathcal{E}+n\omega)}$, while evanescent modes occupy the Floquet channels $n=-n_e,\ldots,-1$ and have imaginary wave vectors $k_n=i\sqrt{2|\mathcal{E}+n\omega|}$. The current density of the evanescent modes is zero. We note that the terms propagating/evanescent modes correspond to what some authors refer to as open/closed channels, respectively. For the Floquet $\boldsymbol{S}$ matrix to be unitary we need to normalize the current density of the propagating modes. To do so, we have introduced the constants $1/\sqrt{k_n}$ in the wave function in Eqs. (18) and (19). To simplify notation in Eqs. (18) and (19), we introduce the constants $1/\sqrt{k_n}$ for the evanescent modes as well, even though they have zero current density.

It is important to note, once again, that the reason we choose to work in the KH frame is that in this frame we can define asymptotic regions where the potential is zero and thus, the Floquet channels are not coupled, in contrast with the scattering region, as we have already shown. The existence of the asymptotic regions guarantees that probability is conserved in the truncated number of Floquet channels and thus the Floquet $\boldsymbol{S}$ matrix is a unitary matrix.

D. Floquet S matrix

The Floquet $\boldsymbol{S}$ matrix connects the outgoing propagating modes with the incoming propagating modes, and in this section we show how to construct it. As we show in what follows, the Floquet $\boldsymbol{S}$ matrix connects channels with energies that differ by an integer multiple of ω, while in the usual time-independent scattering theory the $\boldsymbol{S}$ matrix connects channels with the same energy. The reason is that the Floquet $\boldsymbol{S}$ matrix describes a time-dependent process and thus the energy of the incident electron is not conserved. However, because the Hamiltonian is time periodic, according to Floquet theory [15], the Floquet energy $\mathcal{E}$ defined modulo ω is a conserved quantity.

The wave function and its first spatial derivative must be continuous at the boundaries of the asymptotic regions $\pm x_0$. At $x=x_0$ these conditions lead to

$$b_n^{out}\frac{e^{ik_nx_0}}{\sqrt{k_n}}+b_n^{in}\frac{e^{-ik_nx_0}}{\sqrt{k_n}}$$
$$=\sum_{m=1}^{N}[\chi_{n,m}(x_0)c_m+\chi_{n,N+m}(x_0)d_m], \quad (20)$$

$$ik_nb_n^{out}\frac{e^{ik_nx_0}}{\sqrt{k_n}}-ik_nb_n^{in}\frac{e^{-ik_nx_0}}{\sqrt{k_n}}$$
$$=\sum_{m=1}^{N}[\chi'_{n,m}(x_0)c_m+\chi'_{n,N+m}(x_0)d_m], \quad (21)$$

where $\chi'_{n,m}(x)=d\chi_{n,m}(x)/dx$ and $\chi'_{n,N+m}(x)=d\chi_{n,N+m}(x)/dx$, while at $x=-x_0$ they lead to

$$a_n^{out}\frac{e^{ik_nx_0}}{\sqrt{k_n}}+a_n^{in}\frac{e^{-ik_nx_0}}{\sqrt{k_n}}$$
$$=\sum_{m=1}^{N}[\chi_{n,m}(-x_0)c_m+\chi_{n,N+m}(-x_0)d_m], \quad (22)$$

$$-ik_na_n^{out}\frac{e^{ik_nx_0}}{\sqrt{k_n}}+ik_na_n^{in}\frac{e^{-ik_nx_0}}{\sqrt{k_n}}$$
$$=\sum_{m=1}^{N}[\chi'_{n,m}(-x_0)c_m+\chi'_{n,N+m}(-x_0)d_m]. \quad (23)$$

Due to the connection conditions Eqs. (20), (21), (22), and (23) only $2N$ out of the $6N$ coefficients are arbitrary and we choose those to be the incoming probability amplitudes a^{in} and b^{in}. In Eqs. (20), (21), (22), and (23), the probability amplitudes a^{in} and b^{in} of the evanescent modes are zero because of the unbounded character of the exponentials they multiply in the asymptotic regions I and III. That is, $b_n^{in}=a_n^{in}=0$, for $n=-n_e,\ldots,-1$. We now introduce the $N\times N$ matrices

$$(\boldsymbol{K}_{\pm})_{n,l}=e^{\pm ik_nx_0}\delta_{n,l}, \quad (\boldsymbol{K}'_{\pm})_{n,l}=\pm ik_ne^{\pm ik_nx_0}\delta_{n,l},$$
$$n,l=-n_e,\ldots,0,\ldots,n_p, \quad (24)$$

$$\boldsymbol{J}_{n,l}=\begin{cases}0, & \text{if } n\neq l \text{ and if } n=l=-n_e,\ldots,-1,\\ 1, & \text{if } n=l=0,\ldots,n_p,\end{cases} \quad (25)$$

and

$$\boldsymbol{\mathcal{N}}_{n,l}=\frac{1}{\sqrt{k_n}}\delta_{n,l}, \quad n,l=-n_e,\ldots,0,\ldots,n_p. \quad (26)$$

Also $\boldsymbol{X}_{\pm}^{(1)}\equiv\boldsymbol{X}^{(1)}(\pm x_0)$, $\boldsymbol{X}_{\pm}^{(2)}\equiv\boldsymbol{X}^{(2)}(\pm x_0)$, $\boldsymbol{X}_{\pm}^{(1)'}\equiv\boldsymbol{X}^{(1)'}(\pm x_0)$, $\boldsymbol{X}_{\pm}^{(2)'}\equiv\boldsymbol{X}^{(2)'}(\pm x_0)$, where $\boldsymbol{X}^{(1)'}(x)$ and $\boldsymbol{X}^{(2)'}(x)$ are the derivatives of $\boldsymbol{X}^{(1)}(x)$ and $\boldsymbol{X}^{(2)}(x)$ with respect to the one space dimension x. We also introduce the $N\times 1$ matrices $\boldsymbol{A}_n^{out}=a_n^{out}$, $\boldsymbol{B}_n^{out}=b_n^{out}$, $\boldsymbol{A}_n^{in}=a_n^{in}$, $\boldsymbol{B}_n^{in}=b_n^{in}$. Next, we write Eqs. (20), (21), (22) and (23) in matrix form as follows:

$$\boldsymbol{\mathcal{N}}\boldsymbol{K}_+\boldsymbol{B}^{out}+\boldsymbol{\mathcal{N}}\boldsymbol{K}_-\boldsymbol{J}\boldsymbol{B}^{in}=\boldsymbol{X}_+^{(1)}\boldsymbol{C}+\boldsymbol{X}_+^{(2)}\boldsymbol{D}, \quad (27)$$

$$\boldsymbol{\mathcal{N}}\boldsymbol{K}'_+\boldsymbol{B}^{out}+\boldsymbol{\mathcal{N}}\boldsymbol{K}'_-\boldsymbol{J}\boldsymbol{B}^{in}=\boldsymbol{X}_+^{(1)'}\boldsymbol{C}+\boldsymbol{X}_+^{(2)'}\boldsymbol{D}, \quad (28)$$

$$\boldsymbol{\mathcal{N}}\boldsymbol{K}_{+}\boldsymbol{A}^{out}+\boldsymbol{\mathcal{N}}\boldsymbol{K}_{-}\boldsymbol{J}\boldsymbol{A}^{in}=\boldsymbol{X}_{-}^{(1)}\boldsymbol{C}+\boldsymbol{X}_{-}^{(2)}\boldsymbol{D}, \tag{29}$$

$$-\boldsymbol{\mathcal{N}}\boldsymbol{K}'_{+}\boldsymbol{A}^{out}-\boldsymbol{\mathcal{N}}\boldsymbol{K}'_{-}\boldsymbol{J}\boldsymbol{A}^{in}=\boldsymbol{X}_{-}^{(1)'}\boldsymbol{C}+\boldsymbol{X}_{-}^{(2)'}\boldsymbol{D}. \tag{30}$$

After algebra given in Appendix A we find the Floquet $\boldsymbol{S}$ matrix that connects the outgoing probability amplitudes of the propagating modes to the incoming probability amplitudes of the propagating modes, to be

$$\begin{pmatrix}\boldsymbol{A}_p^{out}\\ \boldsymbol{B}_p^{out}\end{pmatrix}=\begin{pmatrix}\boldsymbol{\mathcal{N}}_{pp}^{-1}\boldsymbol{r}'_{pp}\boldsymbol{\mathcal{N}}_{pp} & \boldsymbol{\mathcal{N}}_{pp}^{-1}\boldsymbol{t}_{pp}\boldsymbol{\mathcal{N}}_{pp}\\ \boldsymbol{\mathcal{N}}_{pp}^{-1}\boldsymbol{t}'_{pp}\boldsymbol{\mathcal{N}}_{pp} & \boldsymbol{\mathcal{N}}_{pp}^{-1}\boldsymbol{r}_{pp}\boldsymbol{\mathcal{N}}_{pp}\end{pmatrix}\begin{pmatrix}\boldsymbol{A}_p^{in}\\ \boldsymbol{B}_p^{in}\end{pmatrix}$$
$$\equiv\begin{pmatrix}\boldsymbol{R}' & \boldsymbol{T}\\ \boldsymbol{T}' & \boldsymbol{R}\end{pmatrix}\begin{pmatrix}\boldsymbol{A}_p^{in}\\ \boldsymbol{B}_p^{in}\end{pmatrix}\equiv\boldsymbol{S}\begin{pmatrix}\boldsymbol{A}_p^{in}\\ \boldsymbol{B}_p^{in}\end{pmatrix}, \tag{31}$$

where the $n_p+1\times n_p+1$ (n_p+1 is the number of the propagating modes) matrices $\boldsymbol{r}'_{pp}$, $\boldsymbol{r}_{pp}$, $\boldsymbol{t}'_{pp}$, and $\boldsymbol{t}_{pp}$ defined in Eqs. (A7) and (A8) of Appendix A connect propagating modes to propagating modes and contain the evanescent mode effect as is shown in Appendix A. Also the $n_p+1\times 1$ matrices $\boldsymbol{A}_p^{in}$ $\boldsymbol{A}_p^{out}$, $\boldsymbol{B}_p^{in}$, and $\boldsymbol{B}_p^{out}$ have elements the amplitudes of the propagating modes and are defined in Eq. (A9) of Appendix A, and the $n_p+1\times n_p+1$ matrix $\boldsymbol{\mathcal{N}}_{pp}$ has elements the normalization constants of the propagating modes and is defined in Eq. (A9) of Appendix A. The matrices $\boldsymbol{R}'$, $\boldsymbol{R}$, $\boldsymbol{T}'$, and $\boldsymbol{T}$ have dimensions $n_p+1\times n_p+1$ and their elements are given in terms of the elements of the $\boldsymbol{r}'_{pp}$, $\boldsymbol{r}_{pp}$, $\boldsymbol{t}'_{pp}$ and $\boldsymbol{t}_{pp}$ matrices as follows:

$$R'_{n',n}=\sqrt{\frac{k_{n'}}{k_n}}(\boldsymbol{r}'_{pp})_{n',n},\quad R_{n',n}=\sqrt{\frac{k_{n'}}{k_n}}(\boldsymbol{r}_{pp})_{n',n},$$

$$T'_{n',n}=\sqrt{\frac{k_{n'}}{k_n}}(\boldsymbol{t}'_{pp})_{n',n},\quad T_{n',n}=\sqrt{\frac{k_{n'}}{k_n}}(\boldsymbol{t}_{pp})_{n',n}, \tag{32}$$

with $n',n=0,\ldots,n_p$.

In Appendix B, we show how to obtain numerically the matrices $\boldsymbol{r}_{pp}$ and $\boldsymbol{t}_{pp}$. The Floquet $\boldsymbol{S}$ matrix has dimensions $2(n_p+1)\times 2(n_p+1)$, see Eq. (31), and is determined by the reflection and transmission amplitudes, $R'_{n',n}$, $R_{n',n}$, $T'_{n',n}$, and $T_{n',n}$, of the propagating modes. The elements $|R_{n',n}|^2$ and $|T_{n',n}|^2$ are the reflection and transmission coefficients, respectively, for an electron wave incident on the propagating channel n from the right that gets scattered to the propagating channel n', while the elements $|R'_{n',n}|^2$ and $|T'_{n',n}|^2$ are the reflection and transmission coefficients, respectively, for an electron wave incident on the propagating channel n from the left that gets scattered to the propagating channel n'.

In this section, we have shown how to construct the Floquet $\boldsymbol{S}$ matrix in the KH frame. The reason we work in the KH frame is that we can define asymptotic regions where the wave function is a superposition of free electron waves. That guarantees that the truncated Floquet $\boldsymbol{S}$ matrix is a unitary matrix, that is, the following condition is satisfied:

$$\sum_{n'=0}^{n_p}[|R_{n',n}|^2+|T_{n',n}|^2]=1, \tag{33}$$

for every incident propagating mode $n=0,\ldots,n_p$. The above condition is a statement of conservation of probability. Also, the Floquet $\boldsymbol{S}$ matrix we construct in the KH frame is isospectral with the corresponding matrix in the Lab frame since a unitary transformation is used to transform from the Lab to the KH frame, see Sec. II A. Finally, the criterion we use to successfully truncate to N Floquet channels is that an electron wave incident on the last propagating Floquet channel $n=n_p$ is not affected by the scattering potential. That is, the transmission coefficient $|T_{n_p,n_p}|^2$ should be equal to one as a function of electron incident energy $E(E=\mathcal{E}+n_p\omega)$ as we discuss in more detail in Sec. III B.

E. Symmetries of the Floquet *S* matrix

The Hamiltonian of the scattering model we consider in the KH frame, Eq. (6), is invariant under the transformation $x\rightarrow -x$ and $t\rightarrow t+T/2$, which is known as generalized parity. Thus, $H(x,t)=H(-x,t+T/2)$ and, therefore, $\Phi(-x,t+T/2)$ is also a solution of Eq. (6). Applying the transformation $x\rightarrow -x$ and $t\rightarrow t+T/2$ to Eqs. (18) and (19) it is easy to show that the Floquet $\boldsymbol{S}$ matrix has the following symmetry:

$$R'_{n',n}=R_{n',n}(-1)^{n'-n},\quad T'_{n',n}=T_{n',n}(-1)^{n'-n},$$

with

$$n',n=0,\ldots,n_p. \tag{34}$$

Thus, if we know the reflection/transmission amplitudes, $R_{n',n}/T_{n',n}$ for electron waves incident from the right using Eqs. (34), we can find the reflection/transmission amplitudes, $R'_{n',n}/T'_{n',n}$ for electron waves incident from the left and vice versa.

III. RESULTS

In this section, the calculations are performed with the values $V_0=0.27035$ a.u. and $\delta=2$ a.u. assigned to the parameters of the inverted Gaussian potential. For these parameters the Gaussian potential supports only one bound state of energy $E_b=-0.1327$ a.u. in the field-free case. The parameters V_0 and δ were chosen so as to describe the behavior of a one-dimensional model negative chlorine ion Cl^- in the presence of a laser field, and are the same as considered in Refs. [11,12,16]. The frequency of the time-periodic field is taken constant and equal to $\omega=0.236$ a.u. for all our calculations. For these values of the parameters V_0, δ, and ω the inverted Gaussian potential has been shown to exhibit stabilization [11,12].

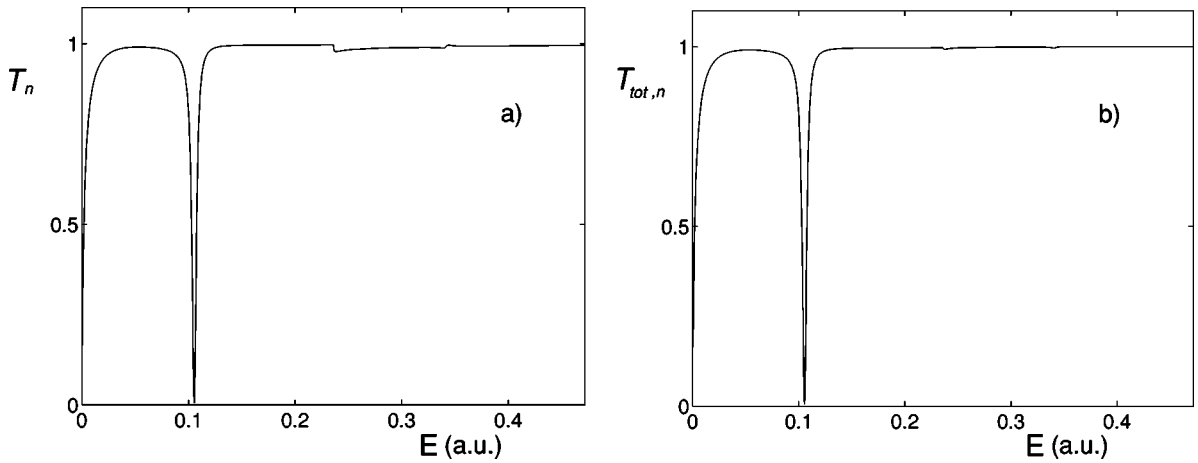

FIG. 3. The transmission coefficients T_n and $T_{tot,n}$, respectively, as a function of electron incident energy E, with $E \in [0,2\omega)$ a.u., for $\alpha_0 = 0.5$ a.u. There is only one Fano transmission resonance at $E = 0.106$ a.u., associated with the first quasibound state.

A. Transmission resonances

In this section, we compute the transmission coefficient T_n and the total transmission coefficient $T_{tot,n}$ as a function of the electron incident energy E, where

$$T_n(E) = |T_{n,n}|^2, \quad T_{tot,n}(E) = \sum_{n'=0}^{n_p} |T_{n',n}|^2,$$

$$E \in [n\omega, (n+1)\omega), \tag{35}$$

with $n = 0,1$. Thus, we consider an electron wave incident from the right with energy $E \in [0,2\omega)$ and compute the transmission coefficients. Keeping the frequency of the time periodic field constant, $\omega = 0.236$ a.u., and varying the strength of the driving field, a_0, we plot the transmission coefficients T_n and $T_{tot,n}$ in Figs. 3, 4, and 5 for α_0 equal to 0.5, 2.25, and 5.25, respectively. The frequency of the driving field $\omega = 0.236$ a.u. is chosen so that it is larger than the binding energy of the ground state $|E_b| = |-0.1327|$ a.u. in the field-free case. The Floquet channels we retain to obtain the numerical results presented in Secs. III A and Sec. III B are $n = -6, \ldots, 0, \ldots, 6$ for $\alpha_0 = 0.5$, $n = -12, \ldots, 0, \ldots, 12$ for $\alpha_0 = 2.25$ and $n = -19, \ldots, 0, \ldots, 19$ for $\alpha_0 = 5.25$, for reasons we discuss in detail at the end of Sec. III B.

The transmission coefficients T_n and $T_{tot,n}$ display sharp asymmetric resonances, as a function of electron incident energy E, that involve a dip or a transmission peak/dip as is shown in Figs. 3, 4, and 5. These asymmetric resonances are due to the interaction of the incident electron wave with the laterally oscillating potential in the KH frame and are the so-called Fano [17,18] type transmission resonances that are known to occur when a bound state is coupled to a continuum of states. This is indeed the case for the scattering model we consider, where the bound state of the inverted Gaussian potential is coupled to a continuum of states through the time periodic electric field. Note in Figs. 3, 4, and 5 that the difference between the transmission coefficient T_n and $T_{tot,n}$ becomes more prominent with increasing α_0. The reason is that as α_0 is increased more Floquet channels interfere with the incident electron wave and significantly

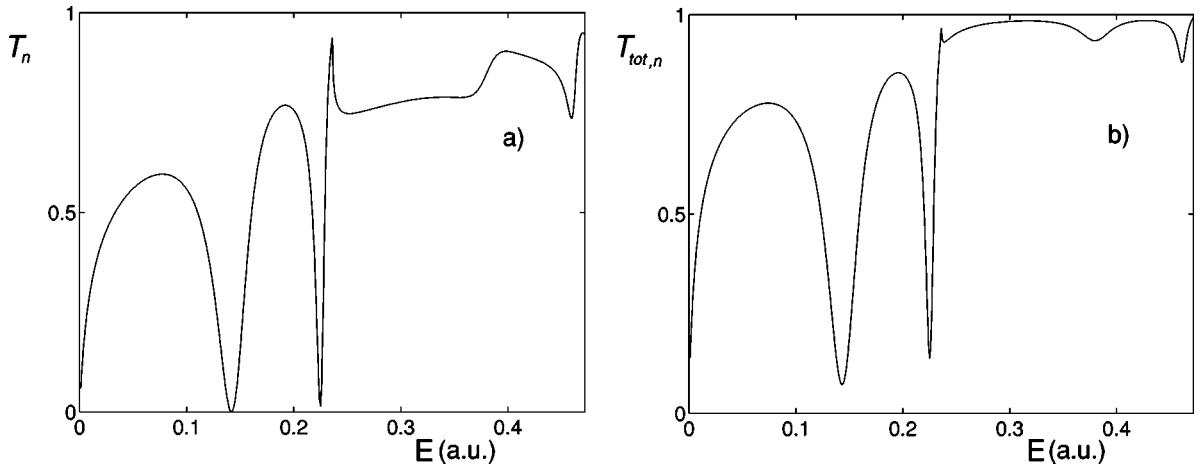

FIG. 4. The transmission coefficients T_n and $T_{tot,n}$, respectively, as a function of electron incident energy E, with $E \in [0,2\omega)$ a.u., for $\alpha_0 = 2.25$ a.u. There are two Fano transmission resonances at $E = 0.142$ a.u. and $E = 0.225$ a.u., associated with the first and second quasibound states, respectively. The second-order Fano transmission resonances for $E > \omega$ are more prominent than those for $\alpha_0 = 0.5$ a.u.

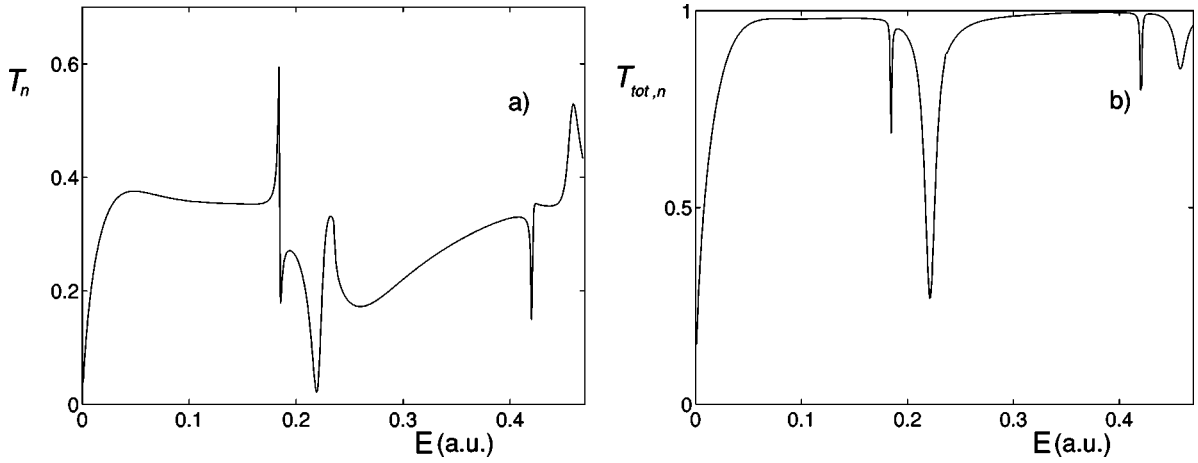

FIG. 5. The transmission coefficients T_n and $T_{tot,n}$ as a function of electron incident energy E, with $E \in [0,2\omega)$ a.u., for $\alpha_0 = 5.25$ a.u. There are two Fano transmission resonances at $E = 0.185$ a.u. and $E = 0.219$ a.u., associated with the first and second quasibound states, respectively. The second-order Fano transmission resonances for $E > \omega$ are more prominent than those for $\alpha_0 = 2.25$ a.u.

contribute to the total transmission coefficient. A comparison of Fig. 3 with Figs. 4 and 5 reveals that as the driving field is increased, the higher-order resonances, for $E > \omega$, become stronger.

We now focus on the transmission coefficient T_n and discuss how it ''probes'' the quasibound states of the system. For $\alpha_0 = 0.5$, see Fig. 3(a), the system has only one Fano transmission resonance, which for small amplitude of the driving field is associated with the $n = -1$ localized Floquet evanescent mode that has its origin in the bound state of the undriven system. When the strength of the driving field is increased, T_n has a second Fano transmission resonance at a higher incident energy, see Figs. 4(a) and 5(a). This second resonance appears for $\alpha_0 > 1$, as was shown in Refs. [11,12], and it is thus a field-induced resonance.

The Fano resonances, which are indicated by a dip or a transmission peak/dip in the coefficient T_n, correspond to quasibound states of the system that show up as poles of the Floquet $\boldsymbol{S}$ matrix in the complex energy plane. In what follows, we compute the poles of T_n in the complex energy plane. Other elements of the Floquet $\boldsymbol{S}$ matrix have poles as well. As was noted in Ref. [19] the asymmetric Fano line shape in T_n is associated with zero-pole pairs when plotting T_n in the complex energy plane. By a zero-pole pair we mean that every transmission zero of T_n along the real energy axis is associated with a pole of T_n on the lower half complex energy plane due to the unitarity of the Floquet $\boldsymbol{S}$ matrix [19]. For $\alpha_0 = 0.5$ there is only one zero-pole pair associated with the single transmission resonance seen in T_n, while for $\alpha_0 = 2.25$ there is a zero-pole pair for each of the two resonances, see Figs. 4(a) and 6. For small strengths of the driving field, $\alpha_0 = 0.5$, the location of the pole on the lower half complex energy plane and of the zero on the real energy axis is the same, while there is a small difference for stronger fields, $\alpha_0 = 2.25$. That is why, we can only approximately determine the real part of the quasibound states from the transmission zeros. From the poles in the complex energy plane, we find the real part of the quasibound states to be $\mathrm{Re}(E_1) = 0.106$, for $\alpha_0 = 0.5$, and $\mathrm{Re}(E_1) = 0.145$, $\mathrm{Re}(E_2) = 0.226$, for $\alpha_0 = 2.25$.

The lifetime τ_L of the quasibound states is determined from the imaginary part of the complex energy, $\mathrm{Im}(E)$, where the pole is found. Then

$$\tau_L = \frac{1}{\Gamma}, \tag{36}$$

where $\Gamma = 2\,\mathrm{Im}(E)$ is the ionization rate. For the inverted Gaussian potential it has been found that with increasing strength of the driving field the ionization rate decreases in an oscillatory manner [11,12]. In Figs. 7 and 8 we show how the real and imaginary part of the quasibound state energies change as a function of α_0, for α_0 ranging from 0 to 6 a.u. The incident particle can emit a photon and drop to a localized Floquet evanescent state. It is in this sense that in Fig. 7

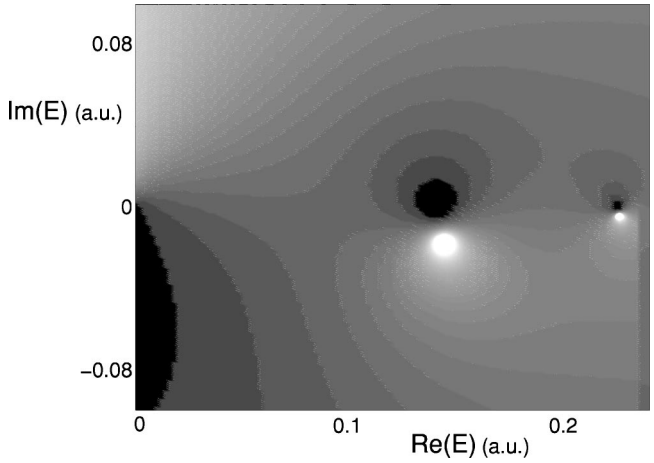

FIG. 6. Contour plot of the transmission coefficient T_n in the complex energy plane for $\alpha_0 = 2.25$ a.u. The dark $\rightarrow$ light areas correspond to increasing values of T_n. There are two zero-pole pairs, each associated with the Fano resonances in Fig. 4. From the poles we determine the real part and the lifetime, τ_L, of the first and second quasibound states.

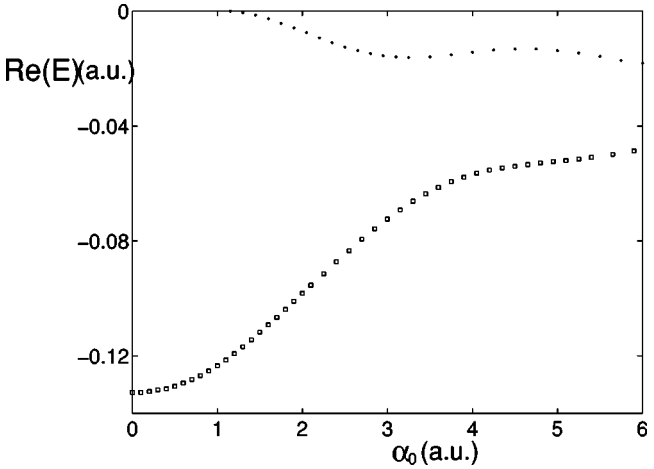

FIG. 7. Real part of the first (squares) and second (dots) quasibound states minus a photon energy as a function of α_0 (a.u.). The real part of the quasibound states is found from the poles of the transmission coefficient T_n in the complex energy plane.

we plot the real part of the quasibound state minus a photon energy and obtain results in agreement with those obtained in Refs. [11,12].

B. Wigner-Smith delay times

Wigner's [20] one-dimensional analysis on time delay in a quantum-mechanical scattering problem was generalized to multichannel scattering by Smith [21] who introduced the Hermitian matrix

$$\hat{Q} = i\hat{S}\frac{d\hat{S}^{\dagger}}{dE}, \tag{37}$$

and interpreted its diagonal elements $\boldsymbol{Q}_{nn}$ as the average delay experienced by a particle incident on the nth channel ($\boldsymbol{S}$ is the unitary scattering matrix).

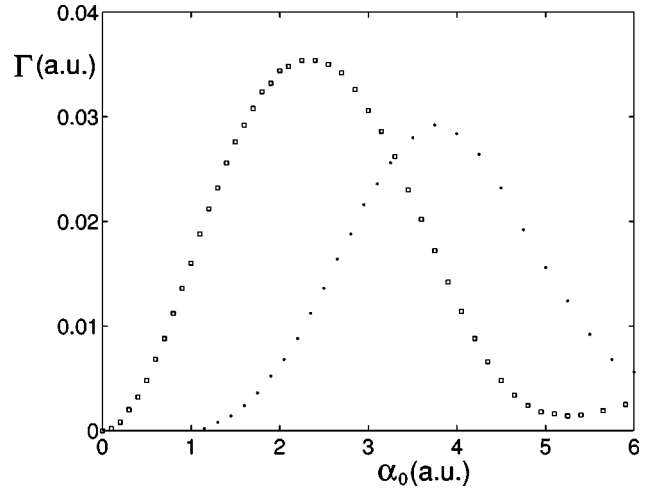

FIG. 8. Ionization rate of the first (squares) and second (dots) quasibound states as a function of α_0 (a.u.). The imaginary part of the quasibound states is found from the poles of the transmission coefficient T_n in the complex energy plane.

In what follows, we compute the diagonal elements of the Wigner-Smith delay matrix $\boldsymbol{Q}$ for the system currently under consideration. We first obtain the eigenvalues and eigenvectors of the Floquet $\boldsymbol{S}$ matrix, see Eq. (31), which is a $2(n_p+1)\times 2(n_p+1)$ matrix when the system is truncated to n_p+1 propagating modes. The $2(n_p+1)$ eigenvalues of the unitary Floquet $\boldsymbol{S}$ matrix have unit magnitude and can thus be cast in the form $e^{i\theta_i(\mathcal{E})}$, where $i=1,\ldots,2(n_p+1)$ and $\theta_i(\mathcal{E})$ is the ith eigenphase as a function of the Floquet energy $\mathcal{E}$. The eigenvector corresponding to the ith eigenvalue $e^{i\theta_i}$ is denoted by $|\theta_i\rangle$. We note that the transmission coefficients T_n and $T_{tot,n}$ (see Sec. III A) as well as the Wigner-Smith delay times τ_{ws}^n, defined in what follows, are a function of incident electron energy $E\in[0,(n_p+1)\omega)$. However, the eigenphases θ_i and the eigenvectors $|\theta_i\rangle$ of the Floquet $\boldsymbol{S}$ matrix are a function of the Floquet energy $\mathcal{E}\in[0,\omega)$ in the sense that if the Floquet energy is defined as the incident electron energy at a higher propagating channel one finds the exact same eigenvalues and eigenvectors. The Floquet $\boldsymbol{S}$ matrix can be written as

$$\hat{S} = \sum_{i=1}^{2(n_p+1)} |\theta_i\rangle e^{i\theta_i}\langle\theta_i|. \tag{38}$$

Each of the eigenvectors $|\theta_i\rangle$ can be expanded in terms of the propagating free electron waves $|k_n\rangle$ that we have used to construct the Floquet $\boldsymbol{S}$ matrix, where $\langle x|k_n\rangle = e^{ik_n x}$. That is, $|\theta_i\rangle = \Sigma_{n=0}^{2n_p+1} p_{n,i}|k_n\rangle$ where $p_{n,i}=\langle k_n|\theta_i\rangle$ and $P_{n,i}=|p_{n,i}|^2$ is the occupation probability of the $|\theta_i\rangle$ eigenvector on the $|k_n\rangle$ propagating channel and $n=0,\ldots,n_p$ for the right-propagating modes and $n=n_p+1,\ldots,2n_p+1$ for the left-propagating modes. The occupation probability of the $|\theta_i\rangle$ eigenvector on a mode incident from the right is the same with that of the corresponding mode incident from the left, that is, $P_{n,i}=P_{n+n_p+1,i}$ for $n=0,\ldots,n_p$. Finally, for each eigenvector $|\theta_i\rangle$ the total occupation probability is normalized to 1, $\Sigma_{n=0}^{2n_p+1}P_{n,i}=1$, where modes incident from the right and the left are taken into account. For modes only incident from the right the normalization for the occupation probability takes the form $\Sigma_{n=0}^{n_p}P_{n,i}=0.5$. From Eqs. (37) and (38) and the fact that the eigenvectors $|\theta_i\rangle$ form a complete set (the Floquet $\boldsymbol{S}$ matrix is unitary) one can show that

$$\langle k_n|\hat{Q}|k_n\rangle \equiv \tau_{ws}^n = \sum_{i=1}^{2(n_p+1)} \frac{d\theta_i}{d\mathcal{E}}\langle k_n|\theta_i\rangle\langle\theta_i|k_n\rangle \Rightarrow \tau_{ws}^n = \sum_{i=1}^{2(n_p+1)} P_{n,i}\frac{d\theta_i}{d\mathcal{E}}. \tag{39}$$

The Wigner-Smith delay times τ_{ws}^n are the average times an electron incident on the nth channel with energy $E\in[n\omega,(n+1)\omega)$ is delayed due to its interaction with the laterally oscillating time-periodic potential in the KH frame. The Wigner-Smith delay times for propagating modes incident from the right are the same with those incident from the left, that is, $\tau_{ws}^n=\tau_{ws}^{n+n_p+1}$ for $n=0,\ldots,n_p$.

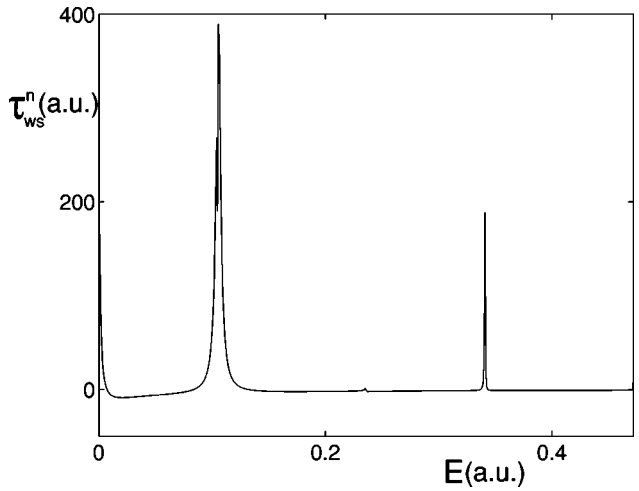

FIG. 9. The Wigner-Smith delay times τ_{ws}^n as a function of electron incident energy $E \in [0,2\omega)$ for $\alpha_0 = 0.5$ a.u. There is one peak at $E = 0.106$ a.u. and smaller peaks at higher-order resonances, associated with the Fano resonance in Fig. 3. For small incident energy E, the Wigner-Smith delay time is positive.

In Figs. 9, 10, and 11 we plot the Wigner-Smith delay times for α_0 equal to 0.5, 2.25, and 5.25, respectively, for modes incident from the right. In Table I, we compare the Wigner-Smith delay times τ_{ws}^n obtained from the Floquet $\boldsymbol{S}$ matrix with the lifetime τ_L obtained from the poles of the T_n transmission coefficient in the complex energy plane and find them to be of the same order of magnitude [22]. At the transmission resonances, the incident electron wave gets trapped by the oscillating potential, populating the quasibound states of the system. The delay of the incident electron wave at the transmission resonances shows up as peaks when plotting the Wigner-Smith delay times as a function of the electron incident energy. Note that as α_0 increases from 2.25 to 5.25 the Wigner-Smith delay time of the 1st quasibound state increases, evidence of stabilization. Another interesting observation is that for small incident energy E the electron has positive Wigner-Smith delay times, for $\alpha_0 = 0.5$, but the electron has negative Wigner-Smith delay times for strong driving fields $\alpha_0 = 2.25$ and 5.25. These latter ones can arise physically either from reflection of the incident electron before it enters the scattering region or from its acceleration and swift passage through the negative potential [21]. In addition, from Figs. 9, 10, and 11 we see, as expected, that when the electron is incident on higher Floquet channels it delays less and less until for very high energies it is not affected by the potential and the delay time is zero.

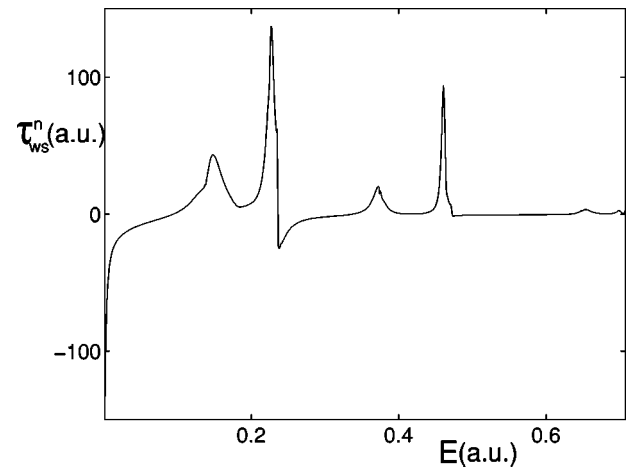

FIG. 10. The Wigner-Smith delay times τ_{ws}^n as a function of electron incident energy $E \in [0,3\omega)$ for $\alpha_0 = 2.25$ a.u. There are two peaks at $E = 0.142$ a.u. and $E = 0.225$ a.u. and smaller peaks at higher-order resonances, associated with the two Fano resonances in Fig. 4. For small incident energy E, the Wigner-Smith delay time is negative.

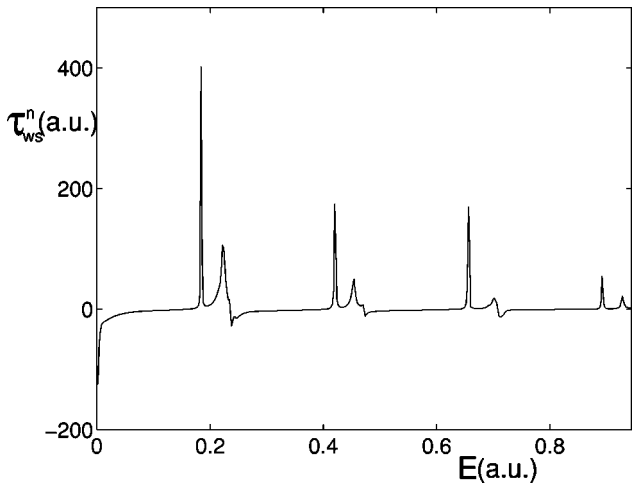

FIG. 11. The Wigner-Smith delay times τ_{ws}^n as a function of electron incident energy $E \in [0,4\omega)$ for $\alpha_0 = 5.25$ a.u. There are two peaks at $E = 0.185$ a.u. and $E = 0.219$ a.u. and smaller peaks at higher-order resonances, associated with the two Fano resonances in Fig. 5. For small incident energy E, the Wigner-Smith delay time is negative.

Now, let us briefly comment on the truncation error of our numerical calculations. The number of Floquet channels N was chosen for each value of α_0 so that the error due to truncation remains small. The truncation error for the elements $R_{n',n}/T_{n',n}$, where $n', n = 0, \ldots, n_p$, is smaller for $n = 0$ and it increases as n approaches n_p, where n_p is the last propagating mode and thus the mode with the larger electron incident energy. Thus, the truncation error for the

TABLE I. The Wigner-Smith delay times τ_{ws}^n compared to the lifetime τ_L for the 1st and 2nd quasibound states for α_0 equal to 0.5, 2.25, and 5.25.

Resonance	τ_{ws}^n (a.u.)	τ_L (a.u.)
$\alpha_0 = 0.5$		
1st resonance	390	208
$\alpha_0 = 2.25$		
1st resonance	43	28.2
2nd resonance	137	104
$\alpha_0 = 5.25$		
1st resonance	244×10	704
2nd resonance	329	81

transmission coefficients T_n and $T_{tot,n}$ computed in Sec. III A is smaller than the error for the Wigner-Smith delay times computed in this section. An estimate of the truncation error is given by $1-|T_{n_p,n_p}|^2$ as a function of incident electron energy. In all our calculations the truncation error is kept in the order of 10^{-4} for $a_0=0.5$, 2.25, and 10^{-3} for $a_0=5.25$ so that our results are reliable. As we increase α_0, we need to consider a larger number of Floquet channels N to maintain a small truncation error in our numerical calculations making it computationally challenging to compute the Wigner-Smith delay times for large values of α_0.

C. Classical-quantum correspondence

When we plot the eigenphases of the Floquet $\boldsymbol{S}$ matrix as a function of the electron Floquet energy $\mathcal{E}$ we notice that the eigenphases undergo an increasing number of ''avoided crossings'' with increasing strength α_0 of the driving field, see Figs. 12, 14, and 15. As we show in what follows, we believe that these ''avoided crossings'' are a quantum manifestation of chaos in the classical phase space.

Let us explain what we mean by the term ''avoided crossing'' in terms of the occupation probabilities, $P_{n,i}$, (defined in Sec. III B) of the $|\theta_i\rangle$ eigenvector on the $|k_n\rangle$ propagating channel. In what follows, we consider the occupation probabilities only for modes incident from the right, that is, $n=0,\ldots,n_p$. In Fig. 12, the eigenphases θ_1 and θ_2 undergo a repulsion when the Floquet energy is equal to the transmission resonance, $\mathcal{E}=0.106$, for $\alpha_0=0.5$. For very small values of α_0 the eigenphases cross each other without repelling. It is only as we increase the strength of the driving field that the eigenphases undergo a repulsion, which we refer to as an ''avoided crossing.'' We describe quantitatively the ''avoided crossing'' between the eigenphases θ_1 and θ_2 in terms of occupation probabilities. In Fig. 13(a), we plot the occupation probabilities $P_{0,1}$, $P_{1,1}$, and $P_{2,1}$ of the $|\theta_1\rangle$ eigenvector on the propagating channels n=0,1,2 and in Fig. 13(b) we plot the occupation probabilities $P_{0,2}$, $P_{1,2}$, and $P_{2,2}$ of the $|\theta_2\rangle$ eigenvector on the propagating channels n=0,1,2 as a function of Floquet energy $\mathcal{E}$. Before the ''avoided crossing,'' $\mathcal{E}<0.106$, $|\theta_1\rangle$ has support mainly on the second propagating channel, $P_{1,1}\approx 0.5$, and $|\theta_2\rangle$ on the first propagating channel, $P_{0,2}\approx 0.5$, while after the ''avoided crossing,'' $\mathcal{E}>0.106$, $|\theta_1\rangle$ has support mainly on the first propagating channel, $P_{0,1}\approx 0.5$, and $|\theta_2\rangle$ on the second propagating channel, $P_{1,2}\approx 0.5$. This total exchange of character is what we refer to as a *sharp* ''avoided crossing.'' Note that for $\alpha_0=0.5$ the propagating channels involved in the ''avoided

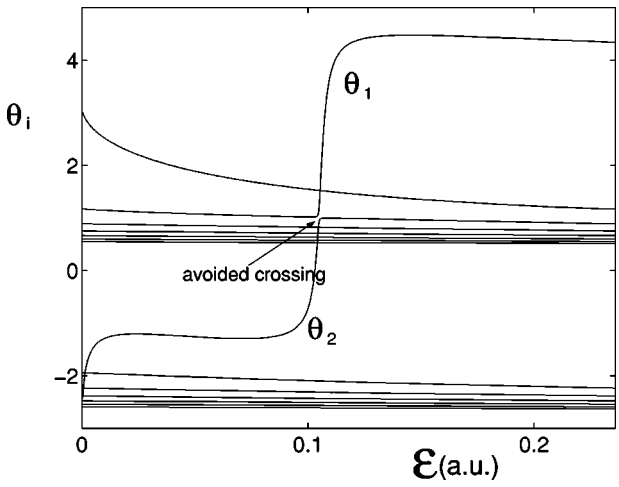

FIG. 12. The eigenphases θ_i (rad) as a function of Floquet energy $\mathcal{E}$ (a.u.) for $\alpha_0=0.5$ a.u. For $a_0\ll 0.5$ a.u. the eigenphases θ_1 and θ_2 intersect each other as a function of Floquet energy $\mathcal{E}$ (a.u.). It is only as α_0 is increased that the eigenphases repel as a function of $\mathcal{E}$ (a.u.) and form an ''avoided crossing,'' indicated by an arrow.

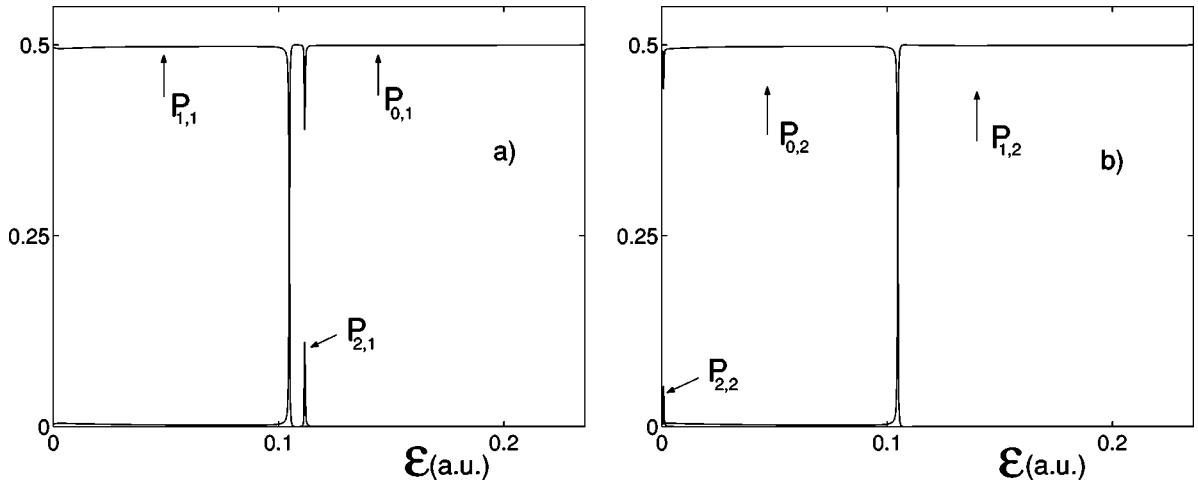

FIG. 13. For $\alpha_0=0.5$, we retain $n=-6,\ldots,0,\ldots 6$ channels and obtain 14 eigenphases from the 14×14 Floquet $\boldsymbol{S}$ matrix. Only two eigenphases θ_1 and θ_2 participate in the ''avoided crossing.'' The eigenphases θ_1 and θ_2 exchange character completely at the sharp ''avoided crossing'' shown in Fig. 12. To show, quantitatively, how the character exchange takes place we plot in (a) the occupation probabilities $P_{0,1}$, $P_{1,1}$, and $P_{2,1}$ of the $|\theta_1\rangle$ eigenvector on the propagating channels $n=0,1,2$ and in (b) the occupation probabilities $P_{0,2}$, $P_{1,2}$, and $P_{2,2}$ of the $|\theta_2\rangle$ eigenvector on the propagating channels $n=0,1,2$ as a function of Floquet energy $\mathcal{E}$ (a.u.). Before the avoided crossing the eigenvector $|\theta_1\rangle$ has support on channel $n=1$ and the eigenvector $|\theta_2\rangle$ mainly on channel $n=0$, while after the avoided crossing the eigenvector $|\theta_1\rangle$ has support mainly on channel $n=0$ and the eigenvector $|\theta_2\rangle$ on channel $n=1$, thus exchanging character completely.

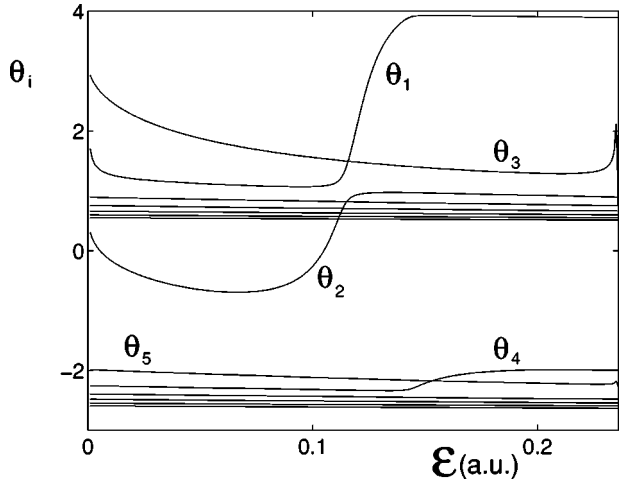

FIG. 14. The eigenphases θ_i (rad) as a function of Floquet energy $\mathcal{E}$ (a.u.) for $\alpha_0=1.25$ a.u. The eigenphases $\theta_1,\ldots,\theta_5$ participate in the ''avoided crossings'' shown in Table II.

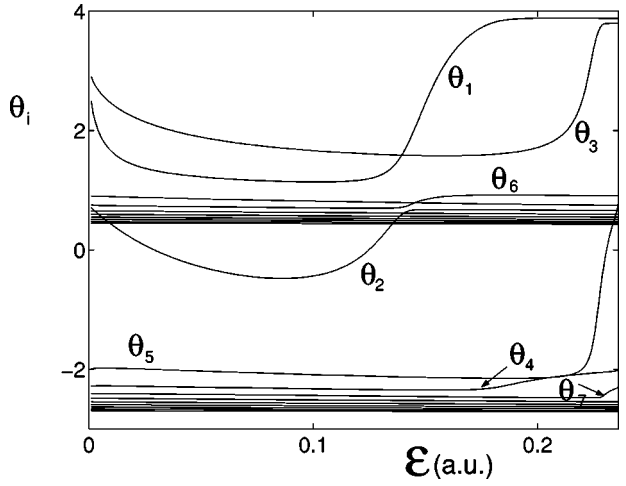

FIG. 15. The eigenphases θ_i (rad) as a function of Floquet energy $\mathcal{E}$ (a.u.) for $\alpha_0=2.25$ a.u. The eigenphases $\theta_1,\ldots,\theta_7$ participate in the ''avoided crossings'' shown in Table III.

crossing'' are mainly $n=0,1$. As the strength of the driving field α_0 is increased an increasing number of propagating channels undergo ''avoided crossings,'' as shown in Tables II and III.

For increased strength of the driving field, the number of avoided crossings increases, see Figs. 14, 15 and it can be that more than two eigenphases participate in an ''avoided crossing'' for a certain Floquet energy. For example, this is the case for the ''avoided crossing'' at $\mathcal{E}\approx 0.14$, for $\alpha_0=2.25$, where there are three eigenphases θ_1, θ_2, and θ_6 interfering, see Fig. 15. In Figs. 14 and 15, we plot the eigenphases of the Floquet $\boldsymbol{S}$ matrix as a function of $\mathcal{E}$ for $\alpha_0=1.25$ and $\alpha_0=2.25$, respectively, to show the increase in the number of ''avoided crossings'' with increasing strength of the driving field. In Tables II and III we present for $\alpha_0=1.25$ and $\alpha_0=2.25$, respectively, the eigephases which undergo ''avoided crossings'' for different Floquet energies $\mathcal{E}$ and the propagating channels $n=0,1,\ldots$ for which the occupation probability $P_{n,i}$ is substantial. In Tables II and III, the channels with small occupation probabilities are indicated as subscripts to the channels with large occupation probabilities. This is only an approximate picture but helps us visualize how the eigenphases change character at the ''avoided crossings.'' For example, from Table III, we obtain an approximate picture how the eigenphases θ_1, θ_2, and θ_6 participate in the ''avoided crossing'' at $\mathcal{E}\approx 0.14$. For $\mathcal{E}=0.07$, the eigenvector $|\theta_1\rangle$ has support mainly on the propagating channel $n=1$ and less on $n=0,2,3$, the eigenvector $|\theta_2\rangle$ has support mainly on the propagating channel $n=0$ and less on $n=1$, the eigenvector $|\theta_6\rangle$ has support mainly on the propagating channel $n=3$ and less on $n=5,1$. For $\mathcal{E}=0.145$, the eigenvector $|\theta_1\rangle$ has support mainly on the propagating channel $n=0$ and less on $n=1$, the eigenvector $|\theta_2\rangle$ has support mainly on the propagating channels $n=1,3$ and less on $n=5$, the eigenvector $|\theta_6\rangle$ has support mainly on the propagating channels $n=1,3$. Thus, there is an exchange of character among the eigenphases θ_1, θ_2 and θ_6 expressed in terms of the mainly interfering channels $n=0,1,3,5$ but it is not a complete exchange as in the case of the *sharp* ''avoided crossing'' at $\alpha_0=0.5$, see Fig. 12. The ''avoided crossings'' we have just described for the open

TABLE II. For $\alpha_0=1.25$ we retain $n=-6,\ldots,0,\ldots,6$ channels and obtain 14 eigenphases from the 14×14 Floquet $\boldsymbol{S}$ matrix. Here we only show the five eigenphases participating in the ''avoided crossings'' at different Floquet energies $\mathcal{E}$, see Fig. 14. For each of the five participating eigenphases $\theta_1,\ldots,\theta_5$ we display the propagating channels $n=0,1,\ldots$ with substantial occupation probability $P_{n,i}$. The propagating channels involved in the ''avoided crossings'' are $n=0,1,2$.

$\mathcal{E}$ (a.u.)	θ_1	θ_2	θ_3	θ_4	θ_5
0.01	0_1	1_0	0	2	1
0.07	1_0	0_1	0	2	1
0.12	0	1	0	2	1
0.15	2	1	0	0	1
0.23	2	1	0_1	0	1_0

TABLE III. For $\alpha_0=2.25$ we retain $n=-12,\ldots,0,\ldots,12$ channels and obtain 25 eigenphases from the 25×25 Floquet $\boldsymbol{S}$ matrix. Here we only show the seven eigenphases participating in the ''avoided crossings'' at different Floquet energies $\mathcal{E}$, see Fig. 15. For each of the seven participating eigenphases $\theta_1,\ldots,\theta_7$ we display the propagating channels $n=0,1,\ldots$ with substantial occupation probability $P_{n,i}$. The propagating channels involved in the ''avoided crossings'' are $n=0,1,\ldots,5$.

$\mathcal{E}$ (a.u.)	θ_1	θ_2	θ_3	θ_4	θ_5	θ_6	θ_7
0.01	$0_{1,2}$	$1_{0,3}$	0_1	2_4	$1_{0,2,3}$	$3_{1,5}$	$3_{1,5}$
0.07	$1_{0_{2,3}}$	0_1	0_{1_2}	2_4	$1_{0,2,3}$	3_{5_1}	$3_{1,5}$
0.145	0_1	$1,3_5$	0_{1_2}	2_4	$1_{0,2,3}$	1,3	$3_{1,5}$
0.18	$2_{0,4}$	$3_{1,5}$	0_{1_2}	0_2	$1_{0,2,3}$	1_3	$3_{1,5}$
0.22	$2_{0,4}$	$3_{1,5}$	1_0	0_{2_1}	0_1	1_3	$3_{1,5}$
0.23	$2_{0,4}$	$3_{1,5}$	$3_{1,5}$	0_{2_1}	0_2	1_3	1_3

quantum system under consideration, the inverted Gaussian in the presence of a driving field, are analogous to what was seen in a bounded chaotic system [23] where the authors also discuss two different types of ''avoided crossings.''

We now turn to the classical dynamics of the inverted Gaussian potential in the presence of the driving field. Figures 16 are strobe plots of the phase-space dynamics, for constant frequency $\omega=0.236$ and increasing strength of the driving field, α_0 is equal to 0.5, 1.25, and 2.25. The strobe plots are drawn by evolving a set of trajectories, with different initial conditions, and plotting the location of each trajectory at time intervals $(t_n=2\pi(m+1/2)/\omega, m=0,1,2\ldots)$ equal to the period of the driving field. We indicate the location of the period-1 periodic orbits with filled squares. The strobe plots are drawn in the Lab frame, see Eqs. (1), (2), and (3), and are exactly the same with those in the KH frame except that in the Lab frame the x axis is shifted by α_0 [24]. If no driving field is present, the motion is regular and bounded for negative energies, while it is unbounded for positive energies. When the driving field is turned on, the KAM tori in the regular island around $x=0$, $p=0$ start breaking up as α_0 is increased and chaotic motion sets in. For $\alpha_0=0.5$, see Fig. 16(a), the classical phase space is mixed. There are two islands around the two stable periodic orbits but there are also chaotic trajectories. As α_0 is further increased the remaining islands are very small, see Fig. 16(b), until they totally disappear, see Fig. 16(c), and the phase space in the scattering region becomes dominated by chaos. In addition, in Figs. 17(a) and 17(b) where the initial values of the classical momenta are chosen to correspond to the middle of the Floquet propagating channels, we find that as α_0 is increased more trajectories get pulled into the chaotic region of the classical phase space. Correspondingly, in the quantum treatment of the scattering problem we have seen that as the strength of the driving field is increased the eigenphases of the Floquet $\boldsymbol{S}$ matrix undergo an increasing number of ''avoided crossings'' where more Floquet channels contribute to the scattering process. We thus believe that the ''avoided crossings'' are a quantum manifestation of the breaking of the constants of motion and chaos setting in in the classical phase space.

IV. CONCLUSIONS

In this paper, we have studied the scattering of electron waves from an inverted Gaussian potential, used to model the atomic potential, in the presence of strong time-periodic electric fields. Using Floquet theory, we have constructed the Floquet $\boldsymbol{S}$ matrix in the KH frame, where asymptotic states can be defined. We have computed the transmission resonances for different strengths of the driving field and shown that they are associated with zero-pole pairs of the Floquet $\boldsymbol{S}$ matrix in the complex energy plane. We have also computed the Wigner-Smith delay times, which is a different way to ''probe'' the complex spectrum of the open quantum system. Finally, we have shown that the eigenphases of the open quantum system undergo a number of ''avoided crossings'' as a function of the electron Floquet energy, that increases with increasing strength of the driving field. We believe that the ''avoided crossings'' are quantum manifestations of the destruction of the KAM surfaces and the onset of chaos in the classical phase space.

ACKNOWLEDGMENTS

We wish to thank the Welch Foundation, Grant No F-1051, NSF Grant No. INT-9602971, and DOE Contract No. DE-FG03-94ER14405 for partial support of this work. We also thank The University of Texas at Austin High Performance Computing Center for use of their computer facilities. Finally, the authors thank A. Gursoy, T. Timberlake, and A. Shaji for helpful discussions.

APPENDIX A

In what follows, starting from Eqs. (27), (28), (29), and (30), we obtain the outgoing probability amplitudes of the propagating modes in terms of the incoming probability amplitudes of the propagating modes.

Using $\boldsymbol{K}_+^{-1}=\boldsymbol{K}_-$ and $\boldsymbol{K'}_+^{-1}\boldsymbol{K'}_-=-\boldsymbol{K}_-^2$, we eliminate $\boldsymbol{B}^{out}$ from Eqs. (27) and (28) and obtain

$$2\boldsymbol{K}_-^2\boldsymbol{J}\boldsymbol{B}^{in}=\boldsymbol{\mathcal{N}}^{-1}\boldsymbol{L}_1\boldsymbol{C}+\boldsymbol{\mathcal{N}}^{-1}\boldsymbol{L}_2\boldsymbol{D}, \tag{A1}$$

where $\boldsymbol{L}_1=\boldsymbol{K}_-\boldsymbol{X}_+^{(1)}-\boldsymbol{K'}_+^{-1}\boldsymbol{X}_+^{(1)'}$ and $\boldsymbol{L}_2=\boldsymbol{K}_-\boldsymbol{X}_+^{(2)}-\boldsymbol{K'}_+^{-1}\boldsymbol{X}_+^{(2)'}$. Using $\boldsymbol{K}_+^{-1}=\boldsymbol{K}_-$ and $\boldsymbol{K'}_+^{-1}\boldsymbol{K'}_-=-\boldsymbol{K}_-^2$, we eliminate $\boldsymbol{A}^{out}$ from Eqs. (29) and (30) and obtain

$$2\boldsymbol{K}_-^2\boldsymbol{J}\boldsymbol{A}^{in}=\boldsymbol{\mathcal{N}}^{-1}\boldsymbol{L}_3\boldsymbol{C}+\boldsymbol{\mathcal{N}}^{-1}\boldsymbol{L}_4\boldsymbol{D}, \tag{A2}$$

where $\boldsymbol{L}_3=\boldsymbol{K}_-\boldsymbol{X}_-^{(1)}+\boldsymbol{K'}_+^{-1}\boldsymbol{X}_-^{(1)'}$ and $\boldsymbol{L}_4=\boldsymbol{K}_-\boldsymbol{X}_-^{(2)}+\boldsymbol{K'}_+^{-1}\boldsymbol{X}_-^{(2)'}$. From Eqs. (A1) and (A2) we express $\boldsymbol{C}$, $\boldsymbol{D}$ in terms of $\boldsymbol{A}^{in}$ and $\boldsymbol{B}^{in}$ as follows:

$$\boldsymbol{C}=2\boldsymbol{G}[\boldsymbol{L}_2^{-1}\boldsymbol{K}_-^2\boldsymbol{J}\boldsymbol{\mathcal{N}}\boldsymbol{B}^{in}-\boldsymbol{L}_4^{-1}\boldsymbol{K}_-^2\boldsymbol{J}\boldsymbol{\mathcal{N}}\boldsymbol{A}^{in}], \tag{A3}$$

$$\boldsymbol{D}=2\boldsymbol{H}[\boldsymbol{L}_1^{-1}\boldsymbol{K}_-^2\boldsymbol{J}\boldsymbol{\mathcal{N}}\boldsymbol{B}^{in}-\boldsymbol{L}_3^{-1}\boldsymbol{K}_-^2\boldsymbol{J}\boldsymbol{\mathcal{N}}\boldsymbol{A}^{in}], \tag{A4}$$

where $\boldsymbol{G}=[\boldsymbol{L}_2^{-1}\boldsymbol{L}_1-\boldsymbol{L}_4^{-1}\boldsymbol{L}_3]^{-1}$ and $\boldsymbol{H}=[\boldsymbol{L}_1^{-1}\boldsymbol{L}_2-\boldsymbol{L}_3^{-1}\boldsymbol{L}_4]^{-1}$. Substituting Eqs. (A3) and (A4) in Eqs. (27) and (29) yields $\boldsymbol{A}^{out}$ and $\boldsymbol{B}^{out}$ in terms of $\boldsymbol{A}^{in}$ and $\boldsymbol{B}^{in}$,

$$\begin{aligned}\boldsymbol{A}^{out}&=\boldsymbol{\mathcal{N}}^{-1}\boldsymbol{r'}\boldsymbol{\mathcal{N}}\boldsymbol{A}^{in}+\boldsymbol{\mathcal{N}}^{-1}\boldsymbol{t}\boldsymbol{\mathcal{N}}\boldsymbol{B}^{in},\\ \boldsymbol{B}^{out}&=\boldsymbol{\mathcal{N}}^{-1}\boldsymbol{t'}\boldsymbol{\mathcal{N}}\boldsymbol{A}^{in}+\boldsymbol{\mathcal{N}}^{-1}\boldsymbol{r}\boldsymbol{\mathcal{N}}\boldsymbol{B}^{in},\end{aligned} \tag{A5}$$

or equivalently

$$\begin{aligned}\boldsymbol{\mathcal{N}}\boldsymbol{A}^{out}&=\boldsymbol{r'}\boldsymbol{\mathcal{N}}\boldsymbol{A}^{in}+\boldsymbol{t}\boldsymbol{\mathcal{N}}\boldsymbol{B}^{in},\\ \boldsymbol{\mathcal{N}}\boldsymbol{B}^{out}&=\boldsymbol{t'}\boldsymbol{\mathcal{N}}\boldsymbol{A}^{in}+\boldsymbol{r}\boldsymbol{\mathcal{N}}\boldsymbol{B}^{in},\end{aligned} \tag{A6}$$

where

$$\begin{aligned}\boldsymbol{r'}&=-[\boldsymbol{K}_-^2+2\boldsymbol{K}_-\boldsymbol{X}_-^{(1)}\boldsymbol{G}\boldsymbol{L}_4^{-1}\boldsymbol{K}_-^2\\&\quad+2\boldsymbol{K}_-\boldsymbol{X}_-^{(2)}\boldsymbol{H}\boldsymbol{L}_3^{-1}\boldsymbol{K}_-^2]\boldsymbol{J},\\ \boldsymbol{r}&=[-\boldsymbol{K}_-^2+2\boldsymbol{K}_-\boldsymbol{X}_+^{(1)}\boldsymbol{G}\boldsymbol{L}_2^{-1}\boldsymbol{K}_-^2+2\boldsymbol{K}_-\boldsymbol{X}_+^{(2)}\boldsymbol{H}\boldsymbol{L}_1^{-1}\boldsymbol{K}_-^2]\boldsymbol{J},\\ \boldsymbol{t'}&=-2[\boldsymbol{K}_-\boldsymbol{X}_+^{(1)}\boldsymbol{G}\boldsymbol{L}_4^{-1}\boldsymbol{K}_-^2+\boldsymbol{K}_-\boldsymbol{X}_+^{(2)}\boldsymbol{H}\boldsymbol{L}_3^{-1}\boldsymbol{K}_-^2]\boldsymbol{J},\end{aligned}$$

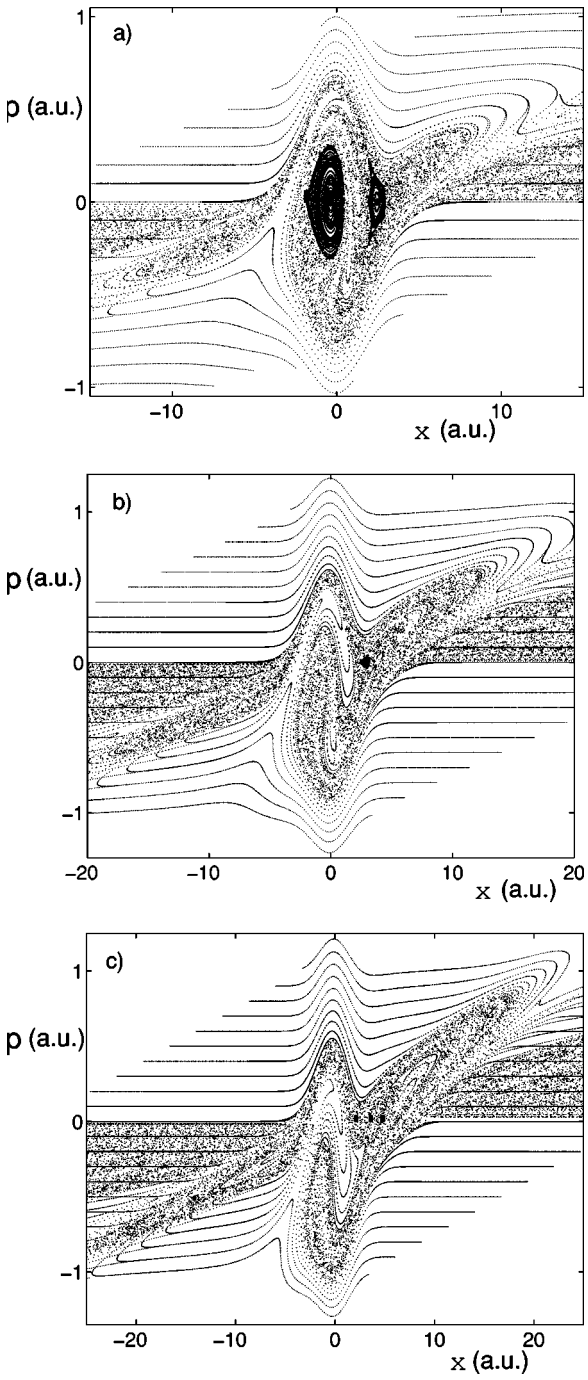

FIG. 16. Strobe plots of the classical dynamics, for the inverted Gaussian in the presence of the driving field, in the laboratory frame for (a) $\alpha_0=0.5$, (b) $\alpha_0=1.25$, and (c) $\alpha_0=2.25$. The initial conditions used to generate the plots lie on the line $p=0$ as well as on the lines with $-1<p<1$. The location of the period-1 orbits are indicated by filled squares. The period-1 orbits are located at (a) -1.87, -0.36, and 2.46; (b) 2.84; and (c) 1.88, 3.38, and 4.54. For very small values of the driving field α_0 (not shown) there is a large regular island around the region at $x=0$, $p=0$. As α_0 is increased to 0.5, there are two regular islands reduced in size indicating the destruction of the KAM tori. As α_0 is further increased to 1.25 and 2.25 the regular islands disappear and the phase space is dominated by chaos.

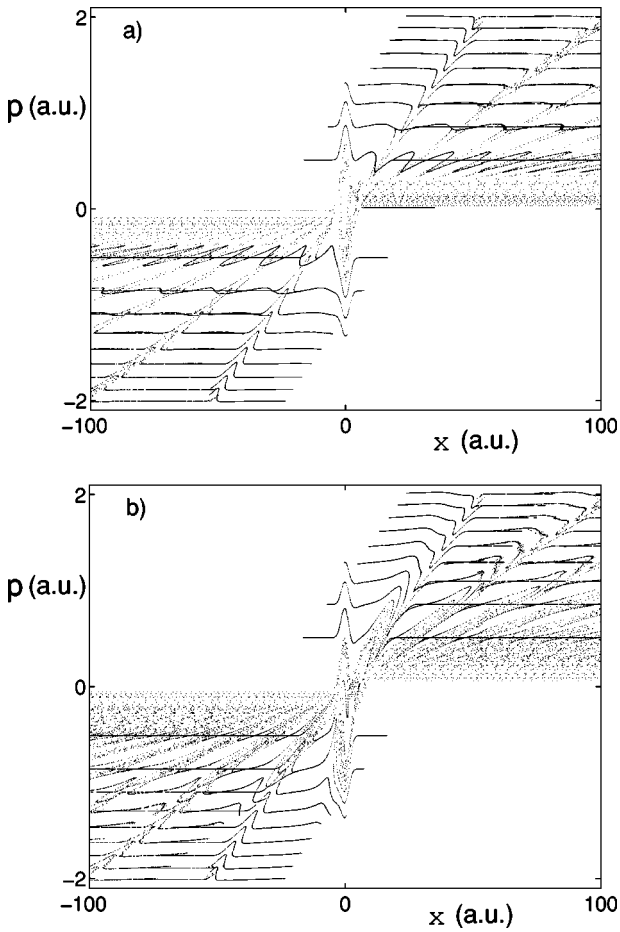

FIG. 17. Strobe plots of the classical dynamics, for the inverted Gaussian in the presence of the driving field, in the laboratory frame for (a) $\alpha_0=0.5$ and (b) $\alpha_0=2.25$. The initial conditions of the classical momenta used to generate the plots are chosen to correspond to the middle of the Floquet propagating channels, that is, the initial conditions lie on the lines $p=\pm\sqrt{2(0.13+n\omega)}$ with $n=0,1,\ldots,8$. As the strength of the driving field is increased more trajectories get pulled in the chaotic region in the classical phase space.

$$\boldsymbol{t}=2[\boldsymbol{K}_-\boldsymbol{X}_-^{(1)}\boldsymbol{G}\boldsymbol{L}_2^{-1}\boldsymbol{K}_-^2+\boldsymbol{K}_-\boldsymbol{X}_-^{(2)}\boldsymbol{H}\boldsymbol{L}_1^{-1}\boldsymbol{K}_-^2]\boldsymbol{J}. \quad \text{(A7)}$$

From Eqs. (A7), due to the multiplication on the right by the $N\times N$ matrix $\boldsymbol{J}$, we find that the $N\times N$ matrices $\boldsymbol{r}'$, $\boldsymbol{r}$, $\boldsymbol{t}'$, and $\boldsymbol{t}$ are of the following form:

$$\boldsymbol{r}'=\begin{pmatrix}\boldsymbol{0}_{ee} & \boldsymbol{r}'_{ep}\\ \boldsymbol{0}_{pe} & \boldsymbol{r}'_{pp}\end{pmatrix},\quad \boldsymbol{r}=\begin{pmatrix}\boldsymbol{0}_{ee} & \boldsymbol{r}_{ep}\\ \boldsymbol{0}_{pe} & \boldsymbol{r}_{pp}\end{pmatrix},\quad \boldsymbol{t}'=\begin{pmatrix}\boldsymbol{0}_{ee} & \boldsymbol{t}'_{ep}\\ \boldsymbol{0}_{pe} & \boldsymbol{t}'_{pp}\end{pmatrix},$$

$$\boldsymbol{t}=\begin{pmatrix}\boldsymbol{0}_{ee} & \boldsymbol{t}_{ep}\\ \boldsymbol{0}_{pe} & \boldsymbol{t}_{pp}\end{pmatrix}, \quad \text{(A8)}$$

where the matrices $\boldsymbol{r}'_{ep}$, $\boldsymbol{r}_{ep}$, $\boldsymbol{t}'_{ep}$, and $\boldsymbol{t}_{ep}$ have dimensions $n_e\times n_p+1$ and the matrices $\boldsymbol{r}'_{pp}$, $\boldsymbol{r}_{pp}$, $\boldsymbol{t}'_{pp}$, and $\boldsymbol{t}_{pp}$ have dimensions $n_p+1\times n_p+1$, respectively (n_e is the number of the evanescent modes and n_p+1 is the number of the propagating modes). The matrices $\boldsymbol{0}_{ee}$ and $\boldsymbol{0}_{pe}$ have dimensions $n_e\times n_e$ and $n_p+1\times n_e$, respectively, and they have zero el-

ements because the amplitudes b^{in} and a^{in} of the evanescent modes are zero, $b_n^{in}=a_n^{in}=0$, for $n=-n_e,\ldots,-1$.

In addition, the matrices $\mathcal{N}$, $\boldsymbol{A}^{in}$, $\boldsymbol{A}^{out}$, $\boldsymbol{B}^{in}$, and $\boldsymbol{B}^{out}$ can be written as

$$\mathcal{N}=\begin{pmatrix}\mathcal{N}_{ee} & \boldsymbol{0}_{ep}\\ \boldsymbol{0}_{pe} & \mathcal{N}_{pp}\end{pmatrix},\quad \boldsymbol{A}^{in}=\begin{pmatrix}\boldsymbol{A}_e^{in}\\ \boldsymbol{A}_p^{in}\end{pmatrix},\quad \boldsymbol{A}^{out}=\begin{pmatrix}\boldsymbol{A}_e^{out}\\ \boldsymbol{A}_p^{out}\end{pmatrix},$$

$$\boldsymbol{B}^{in}=\begin{pmatrix}\boldsymbol{B}_e^{in}\\ \boldsymbol{B}_p^{in}\end{pmatrix},\quad \boldsymbol{B}^{out}=\begin{pmatrix}\boldsymbol{B}_e^{out}\\ \boldsymbol{B}_p^{out}\end{pmatrix}, \tag{A9}$$

where the matrices $\mathcal{N}_{ee}$, $\mathcal{N}_{pp}$ have dimensions $n_e\times n_e$ and $n_p+1\times n_p+1$, respectively. The elements of the $n_e\times 1$ matrices $\boldsymbol{A}_e^{in}$, $\boldsymbol{A}_e^{out}$, $\boldsymbol{B}_e^{in}$, and $\boldsymbol{B}_e^{out}$ are the amplitudes of the evanescent modes. The elements of the $n_p+1\times 1$ matrices $\boldsymbol{A}_p^{in}$, $\boldsymbol{A}_p^{out}$, $\boldsymbol{B}_p^{in}$, and $\boldsymbol{B}_p^{out}$ are the amplitudes of the propagating modes. Using Eqs. (A8) and (A9) we write Eqs. (A6) as follows:

$$\begin{aligned}
\mathcal{N}_{ee}\boldsymbol{A}_e^{out}&=\boldsymbol{r}'_{ep}\mathcal{N}_{pp}\boldsymbol{A}_p^{in}+\boldsymbol{t}_{ep}\mathcal{N}_{pp}\boldsymbol{B}_p^{in},\\
\mathcal{N}_{pp}\boldsymbol{A}_p^{out}&=\boldsymbol{r}'_{pp}\mathcal{N}_{pp}\boldsymbol{A}_p^{in}+\boldsymbol{t}_{pp}\mathcal{N}_{pp}\boldsymbol{B}_p^{in},\\
\mathcal{N}_{ee}\boldsymbol{B}_e^{out}&=\boldsymbol{t}'_{ep}\mathcal{N}_{pp}\boldsymbol{A}_p^{in}+\boldsymbol{r}_{ep}\mathcal{N}_{pp}\boldsymbol{B}_p^{in},\\
\mathcal{N}_{pp}\boldsymbol{B}_p^{out}&=\boldsymbol{t}'_{pp}\mathcal{N}_{pp}\boldsymbol{A}_p^{in}+\boldsymbol{r}_{pp}\mathcal{N}_{pp}\boldsymbol{B}_p^{in}.
\end{aligned} \tag{A10}$$

From Eqs. (A10) we obtain the Floquet $\boldsymbol{S}$ matrix given in Eq. (31).

APPENDIX B

In Secs. II B, Sec. II C, and Sec. II D we have formally constructed the Floquet $\boldsymbol{S}$ matrix in terms of the functions $\chi_{n,j}(x)$, with $n=-n_e,\ldots,0,\ldots,n_p$ and $j=1,\ldots,2N$, which are linearly independent functions in the scattering region II. For the inverted Gaussian potential the functions $\chi_{n,j}(x)$ can only be obtained numerically. In Appendix A, we formally expressed the matrices $\boldsymbol{r}$ and $\boldsymbol{t}$ in terms of the functions $\chi_{n,j}(x)$. Numerically, though, it is not efficient to compute the functions $\chi_{n,j}(x)$. In what follows, we outline the numerical method [9] we use to obtain the $N\times N$ matrices $\boldsymbol{r}$ and $\boldsymbol{t}$ for electron waves incident from the right.

The wave function in the asymptotic regions I and III is given by Eqs. (18) and (19) with $a_n^{in}=0$, since we only consider electron waves incident from the right. We can then write

$$\phi_n(x_0)=b_n^{out}\frac{e^{ik_nx_0}}{\sqrt{k_n}}+b_n^{in}\frac{e^{-ik_nx_0}}{\sqrt{k_n}},$$

$$\phi_n(-x_0)=a_n^{out}\frac{e^{ik_nx_0}}{\sqrt{k_n}}, \tag{B1}$$

with $b_n^{in}=0$ for $n=-n_e,\ldots,-1$. Next, we write Eqs. (B1) in matrix form using Eqs. (24), (25), and (26) as follows:

$$\boldsymbol{\phi}(x_0)=\boldsymbol{K}_+\mathcal{N}\boldsymbol{B}^{out}+\boldsymbol{K}_-\boldsymbol{J}\mathcal{N}\boldsymbol{B}^{in}, \tag{B2}$$

$$\boldsymbol{\phi}(-x_0)=\boldsymbol{K}(-x_0)\mathcal{N}\boldsymbol{A}^{out}, \tag{B3}$$

where

$$\boldsymbol{K}(x)=\begin{pmatrix}e^{-ik_{-n_e}x} & & & & \\ & \ddots & & & 0\\ & & e^{-ik_0x} & & \\ & & & \ddots & \\ & 0 & & & e^{-ik_{n_p}x}\end{pmatrix}. \tag{B4}$$

Using Eqs. (A6) with $\boldsymbol{A}^{in}=0$, we write Eqs. (B2), (B3) as follows:

$$\boldsymbol{\phi}(x_0)=\boldsymbol{K}_+\boldsymbol{r}\mathcal{N}\boldsymbol{B}^{in}+\boldsymbol{K}_-\boldsymbol{J}\mathcal{N}\boldsymbol{B}^{in}, \tag{B5}$$

$$\boldsymbol{\phi}(-x_0)=\boldsymbol{K}(-x_0)\boldsymbol{t}\mathcal{N}\boldsymbol{B}^{in}. \tag{B6}$$

Next, we use Eq. (13) to numerically propagate $\boldsymbol{\phi}(x)$ from $x=-x_0$ up to $x=x_0$ according to the Numerov algorithm [25]. From Eq. (B6), we see that in practice we numerically integrate the $\boldsymbol{K}(x)$ matrix from $x=-x_0$ up to $x=x_0$, since $\boldsymbol{t}$, $\mathcal{N}$ and $\boldsymbol{B}^{in}$ are constant matrices. Let us indicate by $\tilde{\boldsymbol{K}}(x_0)$ the numerically integrated matrix $\boldsymbol{K}(x)$ at $x=x_0$. Then, matching the wave function and its first derivative at $x=x_0$ and using Eqs. (24), we obtain

$$\begin{aligned}
\tilde{\boldsymbol{K}}(x_0)\boldsymbol{t}\mathcal{N}\boldsymbol{B}^{in}&=\boldsymbol{K}_+\boldsymbol{r}\mathcal{N}\boldsymbol{B}^{in}+\boldsymbol{K}_-\boldsymbol{J}\mathcal{N}\boldsymbol{B}^{in},\\
\tilde{\boldsymbol{K}}'(x_0)\boldsymbol{t}\mathcal{N}\boldsymbol{B}^{in}&=\boldsymbol{K}'_+\boldsymbol{r}\mathcal{N}\boldsymbol{B}^{in}+\boldsymbol{K}'_-\boldsymbol{J}\mathcal{N}\boldsymbol{B}^{in},
\end{aligned} \tag{B7}$$

or equivalently

$$\begin{aligned}
\tilde{\boldsymbol{K}}(x_0)\boldsymbol{t}&=\boldsymbol{K}_+\boldsymbol{r}+\boldsymbol{K}_-\boldsymbol{J},\\
\tilde{\boldsymbol{K}}'(x_0)\boldsymbol{t}&=\boldsymbol{K}'_+\boldsymbol{r}+\boldsymbol{K}'_-\boldsymbol{J}.
\end{aligned} \tag{B8}$$

From Eqs. (B8), we find

$$\begin{aligned}
\boldsymbol{r}&=[\tilde{\boldsymbol{K}}(x_0)^{-1}\boldsymbol{K}_+-\tilde{\boldsymbol{K}}'(x_0)^{-1}\boldsymbol{K}'_+]^{-1}[\tilde{\boldsymbol{K}}(x_0)^{-1}\boldsymbol{K}_-\\
&\quad-\tilde{\boldsymbol{K}}'(x_0)^{-1}\boldsymbol{K}'_-]\boldsymbol{J},\\
\boldsymbol{t}&=[\boldsymbol{K}_-\tilde{\boldsymbol{K}}(x_0)-\boldsymbol{K}'^{-1}_+\tilde{\boldsymbol{K}}'(x_0)]^{-1}[\boldsymbol{K}_-^2-\boldsymbol{K}'^{-1}_+\boldsymbol{K}'_-]\boldsymbol{J},
\end{aligned} \tag{B9}$$

where we have used the relation $\boldsymbol{K}_+^{-1}=\boldsymbol{K}_-$. The matrices $\boldsymbol{r}$ and $\boldsymbol{t}$ given by Eqs. (B9) are of the form shown in Eq. (A8) and thus we can extract the matrices $\boldsymbol{r}_{pp}$ and $\boldsymbol{t}_{pp}$. Following Sec. II D, we then obtain the matrices $\boldsymbol{R}$ and $\boldsymbol{T}$. Finally, using the symmetry property of the Floquet $\boldsymbol{S}$ matrix given in Eq. (34) we find the matrices $\boldsymbol{R}'$ and $\boldsymbol{T}'$ for electron waves incident from the left.

[1] M. Gavrila and J. Z. Kaminski, Phys. Rev. Lett. **52**, 613 (1984).
[2] M. Pont, N. R. Walet, M. Gavrila, and C. W. McCurdy, Phys. Rev. Lett. **61**, 939 (1988); M. Pont and M. Gavrila, *ibid.* **65**, 2362 (1990).
[3] K. Burnett, P. L. Knight, B. R. M. Piraux, and V. C. Reed, Phys. Rev. Lett. **66**, 301 (1991); K. C. Kulander, K. J. Schafer, and J. L. Krause, *ibid.* **66**, 2601 (1991); Q. Su, J. H. Eberly, and J. Javanainen, *ibid.* **64**, 862 (1990).
[4] M. P. de Boer, J. H. Hoogenraad, R. B. Vrijen, R. C. Constantinescu, L. D. Noordam, and H. G. Muller, Phys. Rev. A **50**, 4085 (1994); N. J. van Druten, R. C. Constantinescu, J. M. Schins, H. Nieuwenhuize, and H. G. Muller, *ibid.* **55**, 622 (1997).
[5] C. O. Reinhold, J. Burgdörfer, M. T. Frey, and F. B. Dunning, Phys. Rev. Lett. **79**, 5226 (1997).
[6] H. A. Kramers, *Collected Scientific Papers* (North-Holland, Amsterdam, 1956), p. 272.
[7] W. C. Henneberger, Phys. Rev. Lett. **21**, 838 (1968).
[8] L. Dimou and F. H. M. Faisal, Phys. Rev. Lett. **59**, 872 (1987); L. A. Collins and G. Csanak, Phys. Rev. A **44**, R5343 (1991).
[9] R. Bhatt, B. Piraux, and K. Burnett, Phys. Rev. A **37**, 98 (1988).
[10] J. N. Bardsley and M. J. Comella, Phys. Rev. A **39**, 2252 (1989).
[11] G. Yao and S.-I. Chu, Phys. Rev. A **45**, 6735 (1992).
[12] M. Marinescu and M. Gavrila, Phys. Rev. A **53**, 2513 (1996).
[13] T. Timberlake and L. E. Reichl, Phys. Rev. A **64**, 033404 (2001).
[14] W. Li and L. E. Reichl, Phys. Rev. B **60**, 15 732 (1999).
[15] J. H. Shirley, Phys. Rev. **138**, B979 (1965).
[16] A. S. Fearnside, R. M. Portvliege, and R. Shakeshaft, Phys. Rev. A **51**, 1471 (1995).
[17] U. Fano, Phys. Rev. **124**, 1866 (1961).
[18] E. Tekman and P. F. Bagwell, Phys. Rev. B **48**, 2553 (1993).
[19] W. Porod, Zhi-an Shao, and C. S. Lent, Phys. Rev. B **48**, 8495 (1993).
[20] E. P. Wigner, Phys. Rev. **98**, 145 (1955).
[21] F. T. Smith, Phys. Rev. **118**, 349 (1960).
[22] K. Na and L. E. Reichl, Phys. Rev. B **59**, 13 073 (1999).
[23] T. Timberlake and L. E. Reichl, Phys. Rev. A **59**, 2886 (1999).
[24] M. Henseler, T. Dittrich, and K. Richter, Phys. Rev. E **64**, 046218 (2001).
[25] *Methods in Computational Physics*, edited by B. Alder *et al.* (Academic Press, New York, 1966), p. 16.